

Ultra-Homogeneous B₀ field for High-Field Body Magnetic Resonance Imaging with Unified Shim-RF Coils

Hsin-Jung Yang

Cedars-Sinai Medical Center

Fardad Serry

Cedars-Sinai Medical Center

Peng Hu

University of California, Los Angeles

Zhaoyang Fan

University of Southern California <https://orcid.org/0000-0002-2693-0260>

Hyunsuk Shim

Emory University School of Medicine

Anthony Christodoulou

Cedars-Sinai Medical Center <https://orcid.org/0000-0002-9334-8684>

Nan Wang

Cedars-Sinai Medical Center <https://orcid.org/0000-0002-7616-8083>

Alan Kwan

Cedars-Sinai Medical Center

Yibin Xie

Cedars-Sinai Medical Center

Yuheng Huang

Cedars-Sinai Medical Center

John Stager

Cedars-Sinai Medical Center

Waishing Liu

Cedars-Sinai Medical Center

Linda Azab

Cedars-Sinai Medical Center

Richard Handelin

Cedars-Sinai Medical Center

Meng Lu

Cedars-Sinai Medical Center

Ghazal Yoosefian

Cedars-Sinai Medical Center

Meiyun Wang

Henan Provincial People's Hospital

Rohan Dharmakumar

University of California, Los Angeles

Debiao Li

Cedars-Sinai Medical Center

Hui Han (✉ hui.han@cshs.org)

Cedars-Sinai Medical Center

Article

Keywords: high-field magnetic resonance imaging, B0 field homogeneity, Unified shim-RF Coil, noninvasive imaging

Posted Date: August 26th, 2021

DOI: <https://doi.org/10.21203/rs.3.rs-445400/v1>

License:  This work is licensed under a Creative Commons Attribution 4.0 International License.

[Read Full License](#)

1 **Ultra-Homogeneous B₀ field for High-Field**
2 **Body Magnetic Resonance Imaging with Unified Shim-RF Coils**

3
4 Hsin-Jung Yang¹, Ph.D., Fardad Michael Serry¹, M.S., Peng Hu², Ph.D., Zhaoyang Fan³, Ph.D.,
5 Hyunsuk Shim⁴, Ph.D., Anthony G. Christodoulou¹, Ph.D., Nan Wang¹, Ph.D., Alan Kwan¹,
6 M.D., Yibin Xie¹, Ph.D., Yuheng Huang¹, M.S., John Stager¹, B.S., Wai Shing Liu¹, M.S., Linda
7 Azab¹, Richard Handelin¹, B.S., Meng Lu¹, M.S., Ghazal Yoosefian¹, B.S., Meiyun Wang⁵□,
8 M.D., Ph.D., Rohan Dharmakumar¹□, Ph.D., Debiao Li,¹□, Ph.D., Hui Han¹□, Ph.D.

9

10

11 **Affiliations**

12 ¹Biomedical Imaging Research Institute, Cedars-Sinai Medical Center, Los Angeles, CA, USA

13 ²Department of Radiology, David Geffen School of Medicine, & Department of Bioengineering

14 University of California, Los Angeles, California, USA

15 ³Department of Radiology, Keck School of Medicine, University of Southern California, Los

16 Angeles CA, USA

17 ⁴Department of Radiation Oncology, Emory University School of Medicine, Atlanta, GA, USA

18 ⁵Department of Radiology, Henan Provincial People's Hospital & the People's Hospital of

19 Zhengzhou University, Zhengzhou, China.

20

□email: mywang@ha.edu.cn; rohan.dharmakumar@cshs.org; debiao.li@cshs.org; hui.han@cshs.org

1 **Abstract:**

2 High-field magnetic resonance imaging (MRI, 3.0T and above) offers numerous advantages for
3 imaging the human body over lower-field strengths. However, it suffers from unwanted fast
4 spatially-varying main (B_0) fields caused by the susceptibility mismatch at the tissue interfaces.
5 When this is combined with the anatomical complexity of the human body, undesirable image
6 artifacts can become damaging as they can compromise potential image contrasts, limit the use
7 of accelerated imaging, and interfere with clinical interpretation. Consequently, these limitations
8 restrict the effective utilization of high-field body MRI and emphasize the need for a major
9 improvement in B_0 field homogeneity to take full advantage of the ever increased B_0 field. Here
10 we introduce a Unified shim-RF Coil (UNIC) to overcome this existing bottleneck by
11 transcending the conventional low-efficiency, distantly located B_0 shim coils. UNIC allows a
12 shim array to be freely allotted and seamlessly integrated into a standard surface RF coil, thus
13 maximizing both the performances of RF receive sensitivity and effective B_0 shimming. We
14 demonstrate the capacity of the UNIC approach through detailed characterization of the coil
15 design, prototyping a body coil integrating the UNIC features, and conducting in-vivo imaging
16 of deep organs adjacent to the lung. Our studies provide evidence that UNIC enables
17 homogeneous B_0 fields in the liver and the heart, where strong image artifacts are known to
18 occur, and hence facilitate the acquisition of unprecedented image quality in a clinical 3.0T
19 scanner. Further, UNIC's design is practical as it overcomes one of the most, if not the most,
20 critical limitations of the state-of-the-art high-field MRI with minimal changes to the current
21 MRI hardware architecture. Accordingly, the proposed technique offers opportunities for major
22 advancements in noninvasive imaging of deep organs with high-field imaging in a way it has not
23 been possible thus far.

1 **Introduction:**

2 Since the advent of magnetic resonance imaging (MRI) in the 1970s, major leaps in image
3 quality and signal-to-noise ratio (SNR) have come from steady increases in strength of the main
4 magnetic field (B_0): first from 0.5T and 1.5T in the 20th century, and now to 3.0T and 7.0T in
5 the 21st century^{1,2}. However, stronger B_0 also comes with increased (and more difficult to
6 correct) field inhomogeneity, which hampers the image quality as homogeneous B_0 is imperative
7 for correct spatial representation in MRI images³. Although 3.0T scanners have gained high
8 popularity in hospitals, the field inhomogeneity limitations at tissue interfaces in the human body
9 still constitute a central barrier for harnessing the full potential of high-field (3.0T and above)
10 body MRI^{4,5}.

11 Magnetic susceptibility mismatch across tissue interfaces can perturb the uniform magnetic
12 field lines and set up fast spatially-varying B_0 fields. Since this perturbation scales with the B_0
13 field itself, B_0 correction (B_0 shimming) is particularly challenging at high-field MRI³⁻⁶. The
14 impact of these field variations is visualized as image artifacts, which can compromise the
15 clinical interpretation of the images. Larger mismatches (e.g., at air-tissue interfaces) are
16 especially challenging and most evident in the images of the heart and liver (particularly at
17 tissue-lung interfaces). For example, 1.5T cardiac MRI is a key modality for determining cardiac
18 function and myocardial tissue characteristics, despite the fact that 3.0T MRI can provide greater
19 capacity (faster image acquisition, novel image contrast, etc.). The inability to fully advance
20 cardiac MRI to 3.0T in the clinical realm is fundamentally tied to the B_0 field inhomogeneity at
21 the heart-lung interface. In particular, high SNR readouts using balanced steady-state free
22 precession (bSSFP)⁷, endogenous contrast based on T2* MRI⁸, and fast non-Cartesian readout
23 trajectories⁹⁻¹¹ are unreliable with cardiac MRI at 3.0T. Another example concerns echo-planar
24 imaging (EPI) in body imaging. EPI is frequently relied upon for diffusion MRI¹², MR
25 spectroscopic imaging (MRSI)^{13,14}, and blood-oxygenation-level-dependent MRI (BOLD MRI)
26¹⁵. These provide information beyond macroscopic morphology, on tissue microstructure,
27 metabolism, and function, offering unique information associated with various pathological
28 states¹⁶. However, EPI for body imaging at 3.0T is significantly limited by B_0 inhomogeneities,
29 which drives image distortion and signal dropout¹⁷.

30 Hardware-based B_0 shim is the most direct approach to rectify B_0 inhomogeneity¹⁸⁻²⁸. This
31 has been employed in state-of-the-art MR scanners, which utilize 2nd order spherical harmonic
32 (2nd SH) shim coils in the magnet bore (**Fig. 1A**). However, they are distant from the organs of
33 interest and hence ineffective in generating fast spatially-varying shim fields deep in the body. In
34 spite of the recognition of these limitations, this setup has changed little in the past several
35 decades^{29,30}. Meanwhile, major innovations in radiofrequency (RF) coil technology has
36 revolutionized MRI, primarily through the advent of the multichannel RF receive phased array³¹⁻
37³³. The phased array replaced the distant volume RF coils using multiple surface loops closely
38 surrounding the target organs. This has improved RF-receive sensitivity and enabled faster image
39 acquisition schemes such as parallel imaging^{32,34-37} and simultaneous multi-slice imaging^{38,39}. In
40 the past decade, different approaches have been attempted to introduce high-order B_0 shimming
41 in the brain^{18,19,25,40-46}. However, physical limitations, such as inadequate high-order shim field
42 strength and penetration, coil heating with shim current overload, and compromised RF
43 sensitivity, have hampered their applications for deep organ imaging within the body.
44 Furthermore, these methods often require extra hardware with extensive physical footprints,
45 which are incompatible with clinical workflow (long setup times, difficulties with positioning the

- 1 coil within an already tight scanner bore, etc.), and amplify their challenges in clinical
- 2 translation.

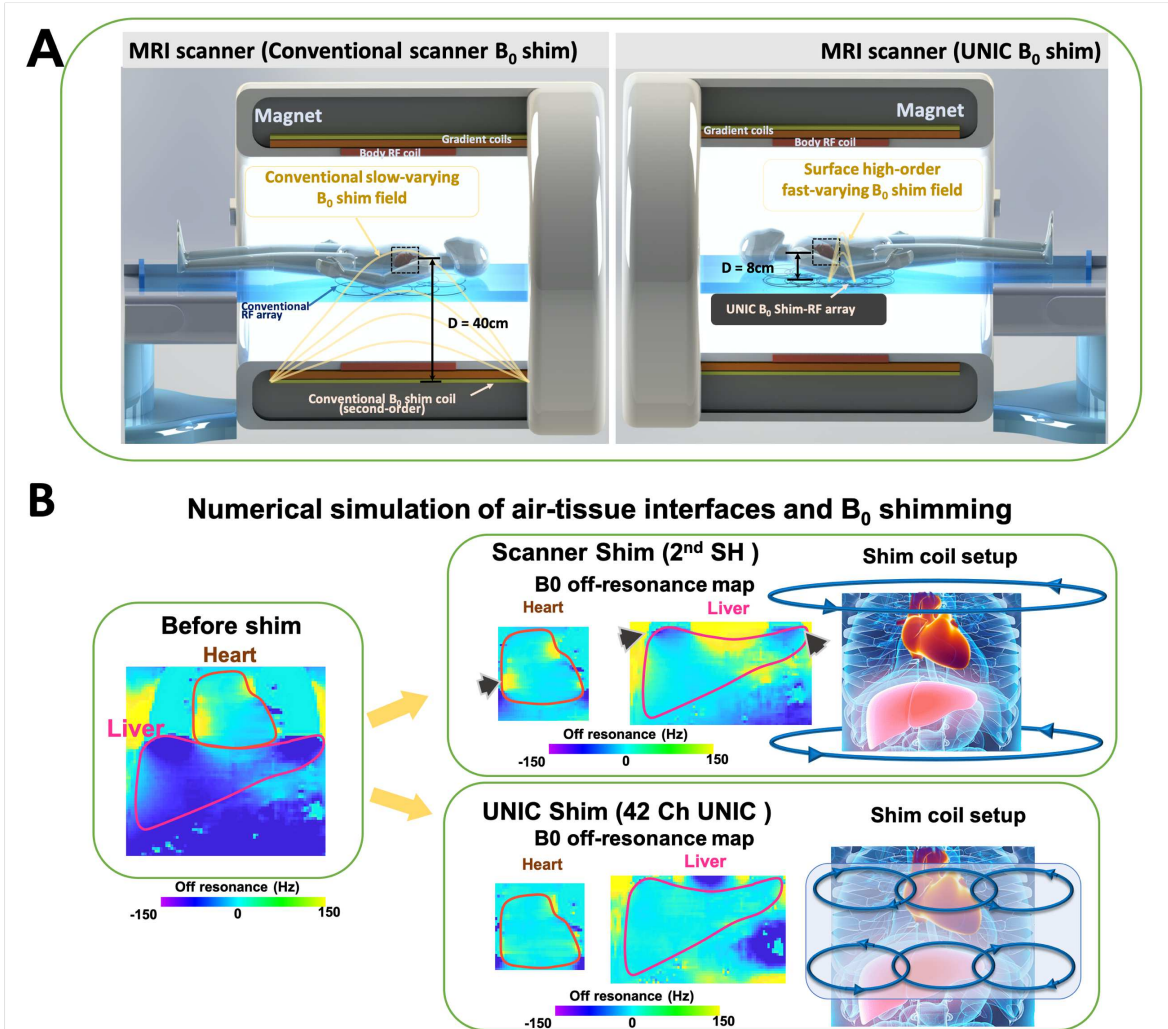


Figure 1 Simulations show that unified shim-RF coil (UNIC) provides more effective B₀ shimming over the state-of-the-art second order spherical harmonic shim. **Panel (A)** illustrates the concept of unified shim-RF coil (UNIC) and its advantages over the state-of-the-art scanner equipped in-bore shim coils. A close distance between the shim loops and the target organ can increase the shim efficiency and efficacy by providing a strong and fast spatially-varying shim field to counteract the inhomogeneous field within the target. For magnetic dipoles (shim coils), the magnetic field strength decreases rapidly with distance (D); proportional to D^{-3} for large distances. When shim coils being placed further away from the target, it would require a dramatic increase of shim current amplitude (I) by I^{+3} and electric power (P) by P^{+6} in order to maintain the same field strength. In practice, the requirements for the excessive high current and power cause the shim efficacy to rapidly decrease with the increasing distance. UNIC reduces the coil-target distance by ~ 5 -fold and increases power efficiency by about 4 orders of magnitude and thus improves the shim efficiency and efficacy compared to in-bore shim coils. **Panel (B)** shows the theoretical simulation of deep tissue shimming with surface shim. The B₀ field map of a virtual patient was shimmed by a standard 2nd order SH in-bore shim coil and 42 channel surface shim coil. The B₀ field inhomogeneities under 2nd SH (black arrows) is substantially reduced under UNIC shim and a more homogenous field is achieved in both organs.

- 3 Here we introduce a Unified shim-RF Coil (UNIC) to address the need for far improved B₀
- 4 shimming for high-field body MRI while avoiding the hardware limitations outlined above.
- 5 Integrating an inherently decoupled surface shim array into a standard RF coil (**Fig. 2A**), UNIC
- 6 maximizes both performances in RF receive and B₀ shimming by minimizing the distances
- 7 between both arrays to the target organs. (**Fig. 1A**) It allows high freedom of shim loop design

1 for strong, high-order shim field penetration, preserves high RF sensitivity, and can be packed
2 into a compact footprint similar to a standard RF coil.

3 In this study, we prototyped the UNIC coil and demonstrated its utility in body MRI at a
4 state-of-the-art 3.0T scanner. We show that the coil vastly improves the image quality of deep
5 organs that are typically hampered by severe B_0 inhomogeneity near the tissue-lung interfaces
6 and successfully reveals pathological lesions that were originally masked by the susceptibility
7 artifacts.

9 The Principle of Unified Shim-RF Coil (UNIC)

10 The working principle and circuit diagram of a typical UNIC element is depicted in **Fig.**
11 **2A&B**. UNIC is composed of a standard RF receive coil (outer loop) and two shim coils (inner
12 loops). The shim coils are connected into a figure-8 shape circuit using two capacitors C_2 . RF
13 currents can thus pass through the capacitors and follow a figure-8 path with DC currents
14 restricted to two separate circular loops. Therefore, each of the shim loops can be independently
15 driven by a separate current source. RF currents induced in the symmetric ‘figure-8’ circuit
16 create magnetic fluxes of equal magnitude but are in opposing directions through the two shim
17 loops, thereby canceling out for the whole circuit. Consequently, the ‘figure-8’ shim circuit and
18 the RF-receive coil are decoupled, having a

19 negligible mutual inductance. The resonant
20 frequency spectrum of a standard RF coil
21 was measured with and without the figure-8
22 shim loops and presented in **Fig. 2D**. A
23 near-identical spectrum was measured with
24 a 3.5% difference in the unloaded quality
25 factor (Q) of the coil shows the high
26 performance of UNIC decoupling. To
27 examine the theoretical performance of
28 UNIC shim in body imaging, computer
29 simulations of B_0 shimming in the heart and
30 liver were performed and compared to the
31 state-of-the-art scanner 2nd SH shim
32 (scanner shim) in **Fig. 1B**. Substantial
33 improvement in B_0 field homogeneity is
34 evident in both organs with UNIC shim
35 enabled by the elimination of the leftover B_0
36 off-resonance under 2nd SH scanner shim
37 (black arrows) at the heart-lung and liver-
38 lung interfaces. Details of the simulation are
39 presented in the Supplementary Material.

40 The UNIC’s inherent decoupling scheme
41 begets its far-reaching consequences for
42 improving B_0 shimming: (1) arbitrary size, shape, position, and number of shim loops create
43 more flexible shim field patterns and fast spatially-varying fields; (2) multiple-turn shim loops
44 multiply field strength and increases tissue penetration depth; (3) reduced shim currents allowed
45 by multi-turn loops and thicker wires relieve heating-related complications; and (4)
46 geometrically decoupled shim-RF circuitry avoids potential SNR loss and image degradation.

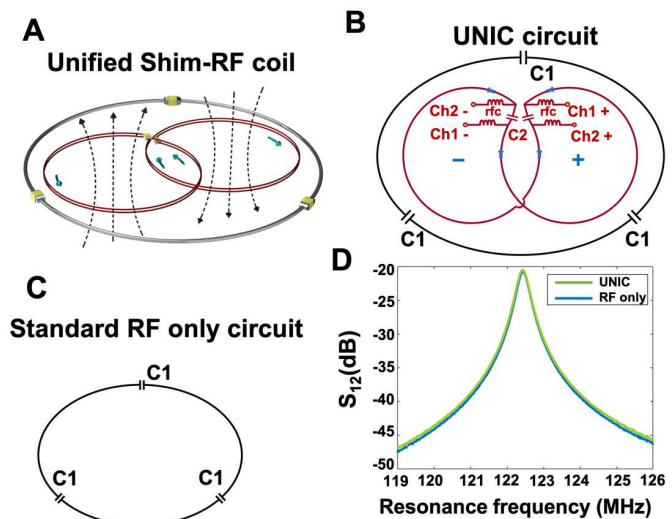


Figure 2 UNIC design preserves RF receive sensitivity of a standard RF only coil. (A) The decoupling mechanism of UNIC. The outer loop is a standard RF receive coil. The figure-8 shape shim coils (inner) are decoupled from the outer RF coil. (B) Circuit diagram of a single UNIC element, comprising an RF receive coil (outer loop) and shim coils (two inner loops connected into a figure-8 shape circuit using two C_2 capacitors). (C) A standard RF receive coil. (D) Plots of the resonant frequency spectrum for a single element UNIC coil and a standard RF receive coil. Excellent decoupling is demonstrated in the UNIC coil with the near-identical spectrums between the UNIC circuit and standard RF circuit.

1 Results

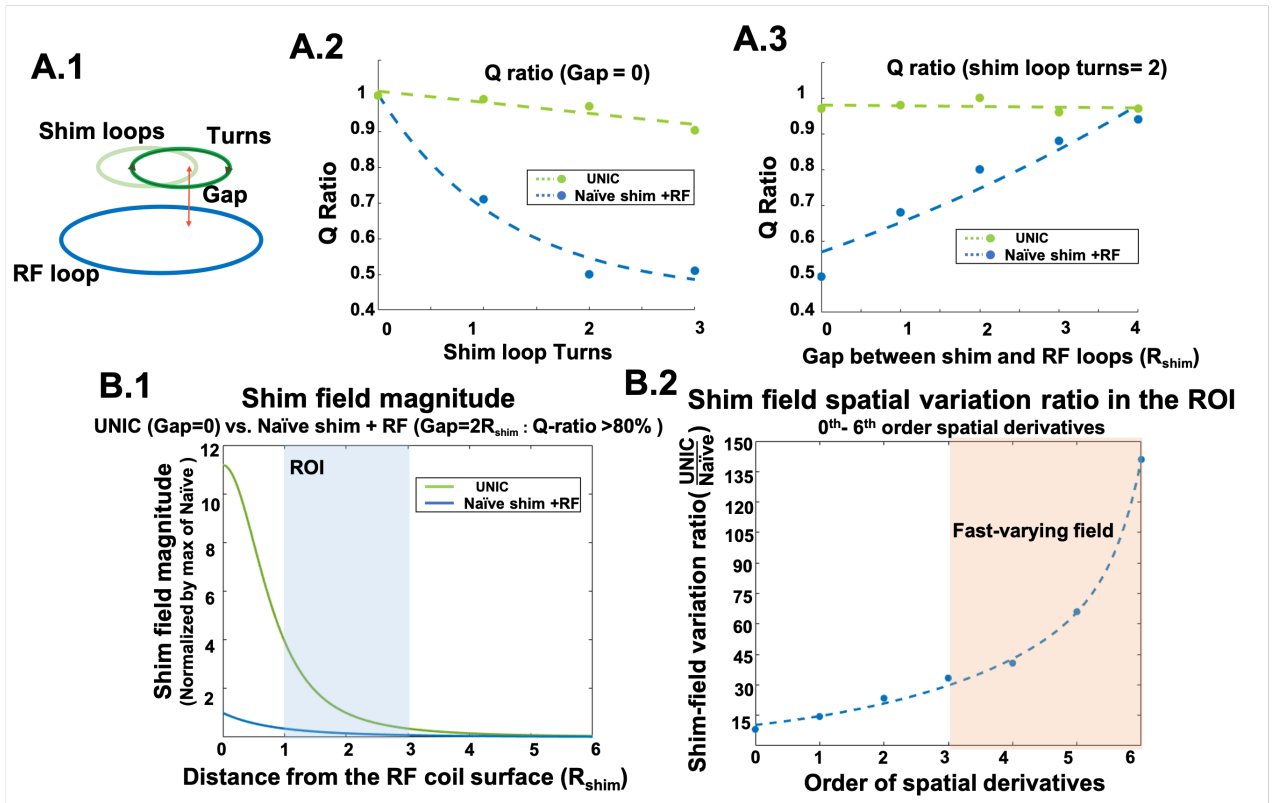
2 To investigate the UNIC design, studies were conducted on the bench, in phantoms, and in-
3 vivo at 3.0T. First, a detailed characterization of the UNIC's SNR preserving property and the
4 amplified fast spatially-varying shim field components were examined on the bench.
5 Subsequently, we constructed a prototype to validate UNIC's imaging capability in a multi-coil
6 setting. Images of the heart and liver (the two major organs that are exposed to the susceptibility
7 artifacts from tissue-lung interfaces) were acquired with sequences that are clinically important
8 and often suffer from off-resonance artifacts (bSSFP cine in the heart and EPI in the liver).
9 Finally, we explored UNIC's benefits in resolving pathological lesions that were originally
10 hidden by off-resonance induced artifacts. Canine models with hemorrhagic myocardial
11 infarctions(hMI) were studied to image the regional iron deposition within the infarction zone
12 using T2* MRI. These studies showed far improved spatial delineation of hemorrhagic zones
13 that were overwhelmed by the off-resonance artifacts without UNIC shim. All studies were
14 conducted in accordance with the Institutional Review Board and the Institutional Animal Care
15 and Use Committee requirements at Cedars-Sinai Medical Center

16

17 UNIC's coplanar shim and RF coils enable strong, fast spatially-varying shim fields deep in 18 the body without compromising RF performance

19 The UNIC RF receive and B₀ shim properties are summarized in **Fig. 3**. The ratio of unloaded-
20 to-loaded quality factors (Q-ratio) was compared in coils with and without UNIC decoupling in
21 panel A. The Q-ratio is a primary parameter of characterizing the RF coil's performance and a
22 main determinant of the image SNR. Two same-size shim loops with 1, 2, and 3 turns were
23 placed in the plane parallel with an RF receive coil. Without UNIC decoupling (naïve coils), Q-
24 ratio was substantially compromised. Compared with the RF-only topology, the Q-ratio for 1, 2,
25 and 3-turn shim loops deteriorated, respectively, 71%, 50%, and 51%. On the other hand, with
26 UNIC decoupling, the same metrics were 99%, 97%, and 90% (**Fig. 3A.2**). One way of reducing
27 SNR loss from RF coupling is by introducing a buffer distance (gap) between the shim and RF
28 loops⁴³. For 2-turn shim loops, Q-ratio variation with buffer distance 0-4 times the shim loop
29 radius R_{shim} (Gap=0-4 times R_{shim}) is shown in **Fig. 3A.3**. Without UNIC decoupling, the Q-ratio
30 was substantially degraded (Q-ratio=50%) when shim loops rested directly on top of the RF loop
31 (Gap=0). At larger buffer distances (Gap>2R_{shim}), Q-ratio recovered passed 80%, but was still far
32 less than when UNIC-decoupled coils were used, resulting in Q-ratio > 96% for all buffer
33 distances.

34 Shim field strength and its spatial derivatives were compared in a region-of-interest (ROI=1-3
35 times R_{shim})⁴⁷ for UNIC (Gap=0) versus the naïve coil with 80% Q-ratio (Gap=2R_{shim}) in **Fig.**
36 **3B**. The shim field drops with the inverse third power of the distance. Therefore in the ROI, the
37 UNIC field strength is on average eight times stronger than the naïve field (**Fig. 3B.1**). Shim
38 field magnitude spatial derivatives (0th-6th order) shown in **Fig. 3B.2** are 33-140 times stronger
39 for UNIC than for the naïve coil. Eliminating the need for a buffer distance, UNIC provides
40 strong, fast spatially-varying fields deep in the body for high-efficiency B₀ shimming.



1
2 **Figure 3** UNIC shim-RF design provides superior RF receive and B_0 shim performances compared to the naïve combination
3 of not decoupled shim and RF coils. UNIC's RF receive performance is characterized on the bench and presented in panel A.
4 (A.1) The geometric configuration of the shim loops and the corresponding RF loop. (A.2.) UNIC maintains a high Q-ratio with
5 multiple-turn shim loops compared to the naïve shim-RF combination. (A.3.) UNIC allows the minimal distance between shim
6 and RF loops without compromising the RF performance compared to the naïve shim-RF combination. UNIC's B_0 shimming
7 property is characterized with numerical simulation in panel B. (B.1) The shim field generated by the UNIC coil (gap=0) versus
8 naïve shim loops (gap= $2R_{shim}$ required to preserve the Q-ratio of over 80% of the RF only loop). The shim field magnitude has a
9 cubic decay dependent on the distance from the coil plane. UNIC has up to a 10-fold increase of the field strength in the region
10 of interest (ROI= $1R_{shim}$ - $3R_{shim}$) versus the naïve loop. (B.2.) The normalized mean magnitude of the shim field in the ROI (ratio
11 of UNIC÷Naïve) at 0^{th} - 6^{th} order spatial derivatives. UNIC greatly increases the efficiency in providing fast spatially-varying
12 fields in the ROI versus the naïve loop (30x and 140x amplification for the 3^{rd} and 6^{th} derivative, respectively).

14 **Prototype UNIC body array provides far improved B_0 shimming and comparable RF** 15 **performance to a state-of-the-art clinical body array coil in phantoms**

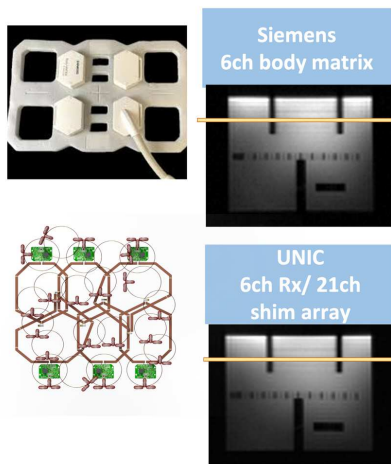
16 To evaluate UNIC's B_0 shim and SNR preserving capability in an array, we evaluated
17 prototypes comprising an in-house built multichannel shim current driver system, 6 RF channels,
18 and 21 evenly distributed two-turn-loop shim coils, against the scanner shimming capability and
19 a similarly-sized standard clinical 6 RF channel body array from the manufacturer (BodyMatrix,
20 Siemens Healthcare).

21 First, absent shim currents, RF receive performances were compared using phantom scans. Inter-
22 element coil correlation matrices and SNRs are shown in **Fig. 4A**. In **Fig. 4A.1**, the UNIC array
23 shows image quality comparable to the clinical array. Also, the similar coil correlation matrices
24 and SNR histogram distributions show UNIC's shim-RF integration did not noticeably degrade
25 RF reception.

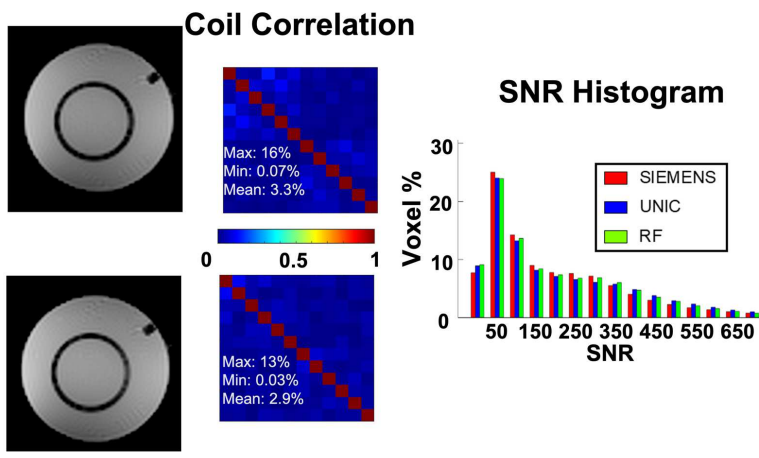
26 Next, we introduced local B_0 perturbation with a metallic object (MO), a copper screwdriver
27 (**Fig. 4B.1**), to test the B_0 shimming capability of the developed coils. Images were acquired
28 with a pair of UNIC arrays at the top and bottom of the phantom. A state-of-the-art image-based

1 shimming procedure was adapted to optimize the 2nd SH shim and UNIC shim.⁴⁸ B₀ field maps
 2 and a bSSFP acquisitions, which are commonly used clinically but are highly sensitive to B₀
 3 field inhomogeneity, were prescribed (**Fig.4.B.2**) with and without UNIC shim. Without UNIC
 4 shim (scanner shim only), a strong residual off-resonance B₀ is implied in the histogram and
 5 evident in the field maps (black arrow). The off-resonance voxels resulted in obvious banding
 6 artifacts in the corresponding bSSFP image (blue arrow). In contrast, UNIC shimming markedly
 7 reduced the off-resonance regions. B₀ homogeneity was significantly improved with the off-
 8 resonance frequencies' 95% range reduced by half (Scanner shim: -33.8 (233) Hz vs. UNIC
 9 shim: 2.2 (82.6) Hz; p<0.01), and a substantially lower root mean square error (RMSE) (UNIC
 10 shim 19.3 Hz vs. Scanner shim: 70.9 Hz). Also, UNIC shimming eliminated banding artifacts in
 11 the bSSFP images.

A.1



A.2



B.1

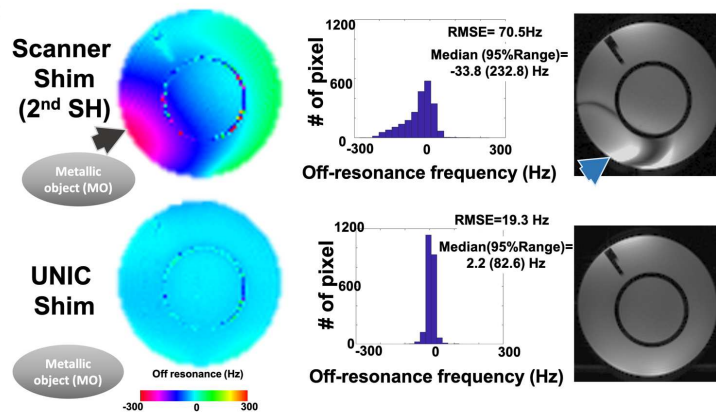
Metallic object with phantom



B.2

B₀ Off-resonance map

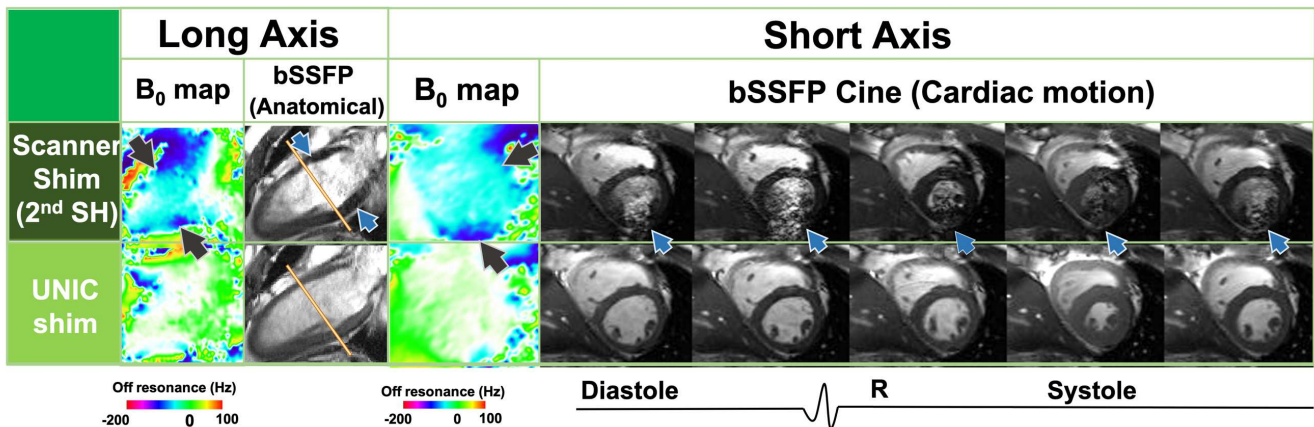
bSSFP



12
 13 **Figure 4 UNIC body coil prototype demonstrates RF-receive performance comparable to a commercially available surface**
 14 **RF-coil and high-order B₀ shimming capability superior to the 2nd SH scanner shim.** Panel A shows the RF receive
 15 performance of the coil prototype. The configuration of a product 6-channel (ch) body RF array and the UNIC array (6-ch RF
 16 receive & 21-ch B₀ shim) (A.1). SNR histograms for three coils with similar geometries: the 6-ch product array, a homemade
 17 conventional 6-ch RF array, and the UNIC array is comparable to the product array. Comparable noise correlation matrix and SNR profile are presented from both
 18 arrays. Panel B shows the validation of the B₀ shim performance of the prototype coil. A metallic object was placed close to an
 19 ACR phantom to introduce a fast-varying B₀ variation (B.1). B₀ field map, B₀ distribution, and bSSFP images using both shim
 20 methods (B.2). A substantially lower RMSE, median, and 95% range was observed after UNIC shim that was accompanied by
 21 vastly improved bSSFP images devoid of banding artifacts.
 22

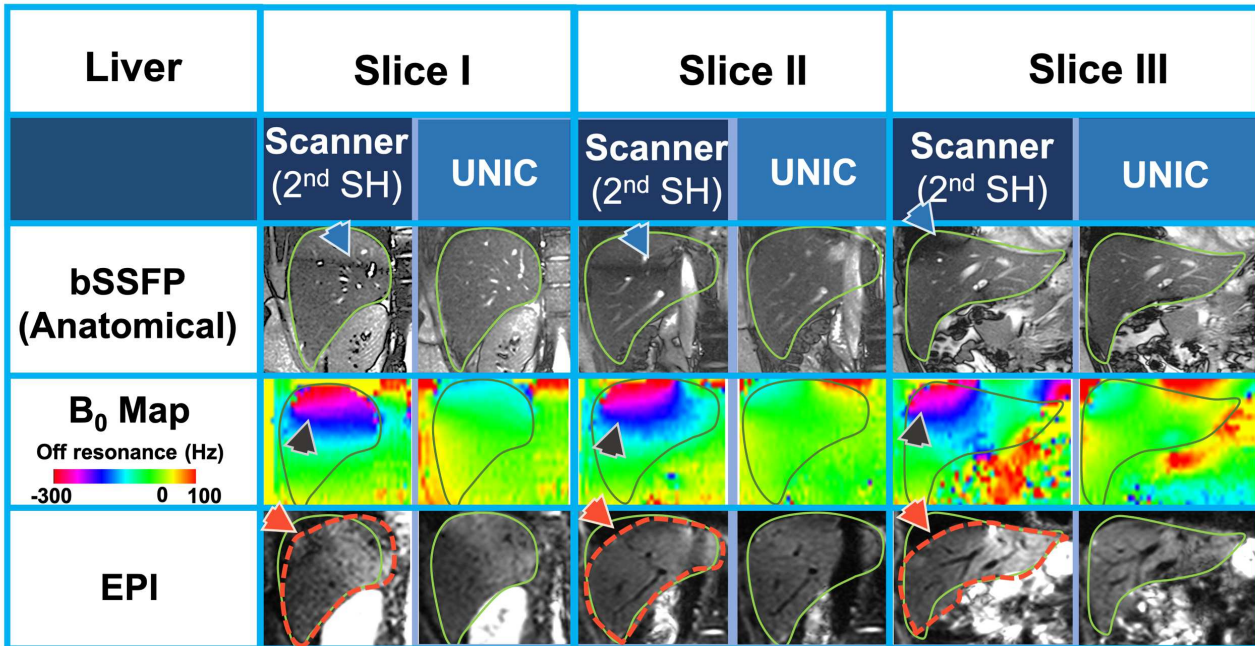
1 **UNIC shimming significantly improves B_0 homogeneity in the human heart and liver,**
 2 **reducing artifacts and rendering more reliable images in a state-of-the-art 3.0T scanner**

3 To validate UNIC's combined shimming/imaging capabilities in-vivo, images of the heart and
 4 the liver were acquired in healthy human volunteers (N=8). In the heart, B_0 field maps, high-
 5 resolution bSSFP long-axis anatomical and short-axis cine images ($1.0 \times 1.0 \text{ mm}^2$, commensurate
 6 with a prolonged repetition time, TR=5.6ms) were acquired to assess UNIC performance under
 7 the highly demanding imaging conditions at 3.0T (**Fig. 5**). State-of-the-art image-based scanner
 8 shim similar to the phantom studies were adopted. Under scanner shim, off-resonance fields
 9 were observed in the B_0 maps on both posterior and anterior of the heart (black arrows). Banding
 10 artifacts at the corresponding locations are shown (blue arrows) and result in significant signal
 11 fluctuation in the myocardium. In the short-axis cine images, banding artifacts interacted
 12 strongly with the ventricular blood, leading to severe smearing artifacts and corrupting all images
 13 across the cardiac cycle ⁴⁹. On the other hand, UNIC shimming substantially improved B_0
 14 homogeneity, eliminating the banding artifacts in both imaging planes. Cine videos are included
 15 in the Supplementary Material.



16
 17 **Figure 5 UNIC shim improves the field homogeneity and image quality in bSSFP cine images of human hearts even at long**
 18 **repetition times.** B_0 field maps and bSSFP images in the heart (long- and short-axis) under scanner shim and UNIC shim are
 19 presented. Under scanner shim, severe B_0 off-resonance were evident at the heart-lung interfaces (black arrows) and were
 20 consistent with the banding artifact (blue arrows) in bSSFP images. Homogeneous B_0 fields and artifact-free bSSFP images were
 21 acquired after applying the UNIC shim.

22
 23 We also performed EPI acquisition of the liver to visualize the liver-lung interfaces. **Fig. 6**
 24 shows representative images of the liver in the coronal view from a healthy human volunteer
 25 under scanner shim and UNIC shim. Under scanner shim, a strong residual off-resonance field
 26 (gray arrows) at the liver-lung interface was evident in all slices, leading to severe artifacts in
 27 both EPI and bSSFP images. The EPI images show geometrical distortion and artifactual signal
 28 intensity fluctuations in the upper segments of the liver (red arrows). These and the banding
 29 artifacts in the bSSFP images (blue arrows) are consistent with the B_0 inhomogeneity patterns. In
 30 contrast, UNIC shimming successfully corrected the high-order off-resonance pattern at the
 31 liver-lung interfaces, substantially reducing artifacts, and leading to improved quality and
 32 enhanced clinical utility of both EPI and bSSFP images in all slices.



2 **Figure 6 UNIC shim markedly improves B_0 field in human livers resulting in significant reductions in imaging artifacts at the**
3 **liver lung interfaces.** B_0 field maps, bSSFP images, and EPI images in the liver following scanner and UNIC shim are shown.
4 Three slices from the posterior to the anterior of the liver were measured to examine the B_0 variations across the whole liver.
5 Following scanner shim, severe B_0 inhomogeneity was observed at the liver-lung interface (black arrows). Corresponding bSSFP
6 images with banding artifacts (blue arrows) and EPI images with geometrical distortion (red arrows) in the corresponding regions
7 are also shown. Following UNIC shimming, it was possible to vastly improve the B_0 field and hence acquire high-quality liver
8 images.

9 **Fig. 7** shows representative histograms of off-resonance B_0 in the liver and the heart. B_0 maps
10 under central frequency tune-up scanner, 2nd order SH scanner, and UNIC shim are shown. The
11 95% range for each histogram was measured to characterize and compare the distributions. The
12 central frequency tune-up field distributions were wide due to native field inhomogeneity in both
13 organs. Although 2nd order SH shim reduced the width, the local fast-varying B_0 inhomogeneity
14 at the tissue-lung interfaces remained, reflected in the asymmetric histograms. UNIC shimming
15 further improved homogeneity, making the histograms more symmetric and about 40%
16 narrower.

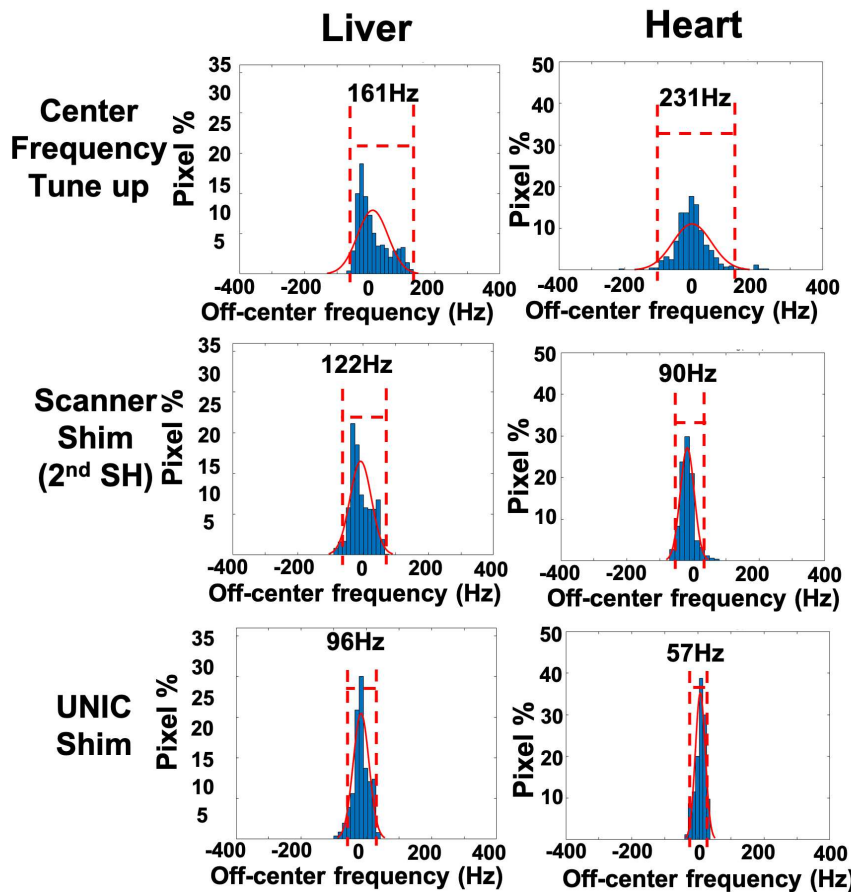


Figure 7 UNIC shimming led to significantly tighter B_0 field distribution compared to the 2nd SH scanner shim in the Heart and Liver. Representative histograms of pixel-wise B_0 field from the heart and the liver in a human subject are shown, which point to significantly narrower B_0 distribution in both the heart and liver following UNIC shim. (Liver: 161Hz (Tune-up) vs. 122Hz (Scanner) vs. 96Hz (UNIC shim); and Heart: 231Hz (Tune-up) vs. 90Hz (Scanner) vs. 57Hz (UNIC)).

12

13 Table 1 shows B_0 homogeneity in-vivo quantified in all subjects using the RMSE, median, 95%
 14 range, and image quality (IQ) scores. Although medians for both 2nd order SH and UNIC shim
 15 were near zero, the RMSE and 95% range were significantly smaller for UNIC. These, together
 16 with UNIC's better IQ scores and the narrower, more symmetric B_0 distributions show the value
 17 of the fast spatially-varying shim field from the UNIC coil. The substantially reduced banding
 18 bSSFP artifacts and corrected EPI geometric distortions see in Fig. 6 UNIC-shimmed images
 19 were observed across all subjects.

20

21 Table 1 Quantitative measurement of off-resonance field distribution and image quality scores in the liver and the heart.
 22 (*denotes $p < 0.05$)

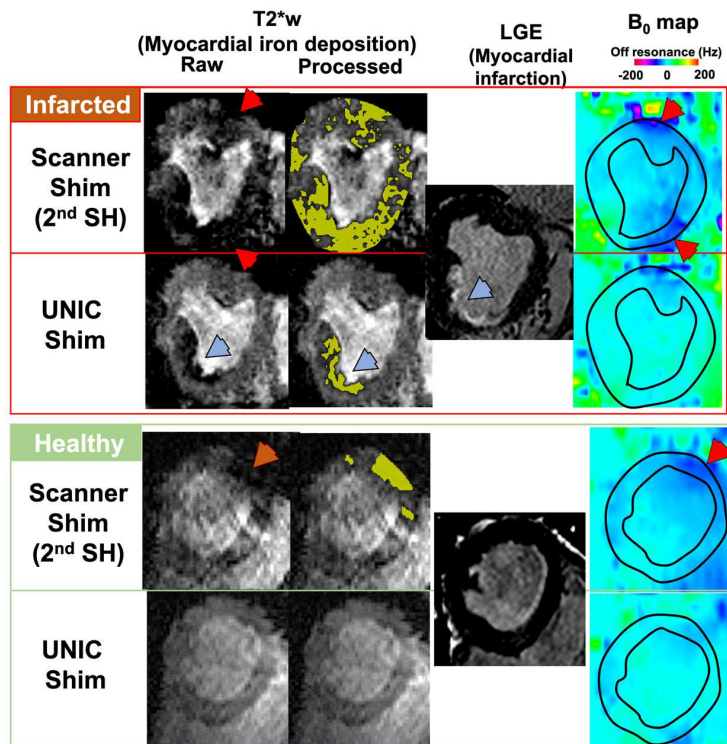
Human (N=8)	Liver					Heart			
	B_0 off resonance (Hz)			EPI IQ score	Anatomical bSSFP IQ score	B_0 off resonance (Hz)			Cine bSSFP IQ score
Distribution parameters	RMSE	Median	95% Range	Mean \pm SD	Mean \pm SD	RMSE	Median	95% Range	Mean \pm SD
Scanner Shim (2 nd SH)	59.8 \pm 19.8	0.5 \pm 8.6	206.6 \pm 58.4	2.9 \pm 0.4	2.2 \pm 0.5	35.3 \pm 15.4	-2.7 \pm 5.3	153.1 \pm 54.7	3.0 \pm 0.4
High-order UNIC Shim	33.4 \pm 8.9*	-0.6 \pm 4.4	128.5 \pm 32.6*	4.3 \pm 0.5*	4.1 \pm 0.7*	21.4 \pm 6.9*	-1.1 \pm 3.8	90.2 \pm 29.0*	4.3 \pm 0.3*

23

1 **UNIC reveals pathological lesions in the heart that were masked by B₀ inhomogeneity**
 2 **artifacts under the state-of-the-art scanner shim.**

3 To investigate UNIC's ability to improve pathological MRI contrast, canine models with and
 4 without hemorrhagic myocardial infarction (hMI) were studied to investigate whether UNIC
 5 shimming can improve visualization of focal myocardial iron deposition.
 6 Focal iron deposition in the heart caused by hMI can lead to life-threatening adverse events⁵⁰⁻⁵⁴.
 7 Recent studies have shown that reliable detection of iron deposition post-myocardial infarction
 8 can play a crucial role in risk stratification and treatment evaluation^{50,51,53}. The ferromagnetic
 9 nature of iron has made T2* MRI the desirable noninvasive method to image myocardial iron
 10 deposition. However, the susceptibility artifacts at the heart-lung interfaces have made reliable
 11 cardiac T2* MRI challenging, particularly at 3.0T^{4,55}. Canines (N=3) with and without hMI
 12 were imaged before and after UNIC shimming. **Fig. 8** shows the T2* images (TE=16.4ms), B₀
 13 off-resonance map, and late-gadolinium enhanced images (LGE) of the myocardium and the
 14 affected territories. T2* images were processed using standard post-processing criteria⁸ to
 15 identify the iron deposition in the hMI region. The detected hMI territories were highlighted with
 16 an olive-color overlay. In all animals, large hypointense artifacts (known as blooming artifacts)
 17 at the heart-lung interfaces were evident in the T2*-weighted images under the scanner shim (red
 18 arrows). The location of the artifacts corresponded closely to the off-resonance pattern from the
 19 B₀ maps (red arrows) and compromised the T2* images reliability for identifying the presence of
 20 iron deposition. The UNIC shim substantially improved the field homogeneity and T2* image
 21 quality. In both healthy and diseased animals, UNIC clearly revealed the left ventricle, originally
 22 masked by the blooming artifacts. In animals with hMI, iron deposition in the infarcted territory
 23 (blue arrows) was clearly identifiable after UNIC shimming and was delineated consistent with
 24 the infarct territory after post-processing. The improved image quality under UNIC shimming
 25 eliminated the false positive regions (red arrows) from the state-of-the-art scanner shimming.
 26 The results demonstrated UNIC's potential for improving the robustness of T2* images for
 27 detecting hMI.
 28

29 **Figure 8 UNIC improves T2* cardiac MRI**
 30 **from canines with and without hemorrhagic**
 31 **myocardial infarction.** Images were acquired
 32 in healthy and infarcted animals with 2nd
 33 order SH and UNIC shims. Hemorrhage-
 34 sensitive T2* images, B₀ field maps, and LGE
 35 images from representative animals with and
 36 without infarction are shown. T2* images
 37 were processed with standard thresholding to
 38 detect myocardial hemorrhage (olive-color
 39 overlay). Following scanner shim, B₀ maps
 40 showed strong B₀ inhomogeneity at the heart-
 41 lung interfaces. Blooming artifacts were
 42 evident in the corresponding regions with
 43 strong B₀ inhomogeneity in the T2* images
 44 (red arrows), which lead to overestimation of
 45 iron-rich regions in the infarcted animal and
 46 false detection of iron in the benign animal
 47 (second column). Following UNIC shim, B₀
 48 field and T2* image quality were significantly
 49 improved, which enabled clear boundaries of
 50 the hemorrhage within the infarcted
 51 myocardium (blue arrows).



1 Discussion

2 Since the introduction of 3.0T scanners for clinical use two decades ago, there have been high
3 expectations that its SNR advantages and increased spectral separation between chemical
4 substances (e.g., fat, water and metabolites) relative to 1.5T would revolutionize body MRI as it
5 has for neuroimaging. Despite years of efforts and various technical improvements, the adoption
6 of 3.0T body MRI is still hampered by the imaging artifacts. B_0 field inhomogeneity is a major,
7 if not the most important, challenge that limits high-field body MRI from advancing to its full
8 potential at 3.0T. The proposed UNIC coil provides an opportunity to impart a strong and fast
9 spatially-varying shim field deep in the body with minimal changes required to the current MRI
10 hardware architecture. Its direct and efficient design allows the utilization of similar mechanical
11 footprints to the standard RF coils, which provides a practical solution for scanner integration.
12 Our studies reveal that UNIC could significantly improve field homogeneity in deep organs that
13 suffer the most from B_0 off-resonance artifacts. We demonstrated that adequate B_0 homogeneity
14 at a clinical 3.0T scanner is achievable in the heart and the liver to correct for undesirable
15 imaging artifacts, including signal nulling, geometrical distortion, motion smearing, and T_2^*
16 blooming. The potential of translating the improved image quality for clear visualization of
17 pathological lesions was demonstrated in an animal model with hemorrhagic myocardial
18 infarction.

19 A homogeneous B_0 field is critical for the advancement of body MRI at 3.0T and above,
20 particularly for increasing SNR efficiency, enabling image contrasts with advanced functional
21 information, providing reliable quantitative multiparametric maps for tissue characterization, and
22 taking full advantage of image acceleration methods or further improving spatial resolution.
23 Taking cardiac MRI for example, since the heart is constantly moving and located deep in the
24 body, it demands high SNR and short acquisition time. The introduction of the highly SNR
25 efficient bSSFP sequence in the early 2000s ⁷ revolutionized cardiac MRI at 1.5T. However, due
26 to high sensitivity to B_0 inhomogeneity, its use for clinical application at 3.0T has been severely
27 hindered because of inconsistent image quality (banding artifacts and biased relaxation values).
28 It has been reported that with the scanner's 2nd SH shimming capabilities, the signal variation at
29 1.5T can be reduced to less than 15% with no banding artifacts at the steady-state ⁶. However,
30 since the off-resonance frequency doubles at 3.0T ⁵⁶, severe banding artifacts can increase the
31 undesirable signal variation to as much as 80% from the truth ⁵⁷. These artifacts can be an
32 impediment for fast imaging techniques using non-Cartesian k-space trajectories such as radial
33 and spiral sampling and lead to the inability to deploy accelerated imaging techniques ⁹⁻¹¹.
34 Similar limitations are presented at the liver-lung interface in EPI readouts, which result in
35 misleading geometrical distortion and signal dropouts ⁵⁸. Due to these difficulties, GRE
36 acquisitions are usually used at 3.0T for body imaging, which are markedly less SNR/CNR
37 efficient and negate its advantages over 1.5T ^{55,59}. In addition, inhomogeneous B_0 can
38 compromise important image contrast that ties to the higher field strength. For example, T_2^* and
39 susceptibility contrasts can be enhanced by the increased susceptibility-induced field changes
40 and allow high-field MRI to improve detection of iron deposition ^{51,60}, myocardial hemorrhage
41 ⁶¹, and oxygen consumption ^{62,63}. Also, the spectral peak separation between metabolites
42 increases proportionally to the field strength, which can boost the CNR in metabolic imaging
43 techniques, including chemical exchange saturation transfer ⁶⁴ and spectroscopy ⁶⁵, and allow
44 better fat-suppression and fat-water separation ^{5,57}. The amplified B_0 inhomogeneity can lead to
45 strong blooming artifacts and spectral corruption, which limits application at high field strengths.
46 Moreover, the growing appreciation of quantitative MRI has further enhanced the importance of

1 B_0 field uniformity. For example, accurate myocardial T1 and T2 maps play important role in
2 assessing ischemic and non-ischemic heart diseases⁶⁶⁻⁶⁹. Because absolute values are reported,
3 B_0 off-resonance can confound the underlying source images and impair the accuracy of the
4 maps and mimic disease^{10,70}. We showed that UNIC can reduce the range of B_0 off-resonance
5 frequencies by more than 40% in the target organs, which has the potential to translate robust
6 body MRI protocols established at the 1.5T to the 3.0T and allows for exploring the full potential
7 from the increased field strength.

8 Over the years, various attempts have been made to improve B_0 homogeneity for high-field
9 MRI. In order to mitigate the loss of efficiency from the cubically decaying magnetic field of
10 magnetic dipoles, methods have been proposed toward bringing the shim coils closer to the
11 subjects to provide stronger shim fields with faster spatial variations. Juchem et al.⁴³
12 implemented a non-decoupled multi-coil shim array arranged near and with a buffer distance
13 (gap) from the RF receive coil to perform local shimming of the brain. However, the requirement
14 for the buffer distance led to critical limitations (as illustrated in **Fig. 3**), which led to an
15 insufficient fast spatially-changing field in deep tissue and compromised RF receive sensitivity
16 and transmit efficiency due to electromagnetic coupling. More importantly, the requirement for
17 the excessive extra space in the already tight scanner bore made it difficult for body shim. Han et
18 al.¹⁸ have attempted to close the gap between shim coils and the subject by creating a DC
19 current path on conventional RF receive loops^{44,45}. However, limited by the single-turn setting,
20 the dual DC-RF operation in the shared conductor can produce hazardous heat when desired high
21 currents for deep shimming are loaded. It also restricts the shim loop geometry by the
22 corresponding RF loops, which hampered the degrees of freedom in the generated shim patterns.
23 Further, a significant loss in coil Q-ratio and sensitivity was reported⁴⁵ by adding extra
24 electronics to the receive loops, which further compromises the image SNR in deep organs.
25 These limitations made the DC-RF setup ineffective in overcoming the challenge of shimming
26 the deep organs. In comparison, UNIC enables strong, deep, high-order B_0 shim by eliminating
27 the critical physical limitations associated with DC-RF shim loops, including size, shape,
28 position, the total shim channel number, the loop turns (1-turn), and wire diameter of the shim
29 loops, as well as SNR degradation.

30 In this proof-of-concept study, rigid flat coils were constructed to facilitate the validation of
31 the UNIC theory in a stationary setup. The anterior UNIC coil was unable to closely surround the
32 body contour as a semi-flexible product coil would do, which can create spacing between the
33 coils and the subject at the peripheral of the field of view and result in suboptimal receive and B_0
34 shim performances. Yet, owing to the intrinsic decoupling scheme, UNIC is adaptable to semi-
35 flexible or flexible RF coils⁷¹⁻⁷⁴, where soft electronics can be employed. A potential
36 complication in using a flexible UNIC coil is that the subject movement may lead to shim field
37 deformation during image acquisition and results in erroneous B_0 shim. To correct for the
38 motion-induced error, previously developed motion extraction techniques^{10,75} can be adopted to
39 estimate the motion during image acquisition and correct the shim fields. Since the goal of the
40 current study was to build a general-purpose coil, evenly distributed shim loops were adopted.
41 Higher shim efficiency and efficacy for specific applications are expected with further
42 optimization of the coil geometry.

43 **Outlook**

44 The study addresses a longstanding unmet challenge with 3.0T body MRI by overcoming the
45 primary limitation in B_0 homogeneity. The proposed advancement here opens the door for
46 multiple new opportunities in body imaging previously out of reach due to inhomogeneous B_0

1 fields. Notably, it can have a major impact in accelerating the clinical adoption of cardiac MRI
2 and EPI-based body imaging at 3.0T. We envision that the technique is scalable across a range of
3 field strengths (e.g., 3.0T and 7.0T) and organs (e.g., brain, neck, and spine). A numerical
4 simulation of a UNIC 7.0T body array with more shim loop turns is presented in the
5 supplementary material with comparable B_0 homogeneity improvement from 3.0T. In addition,
6 UNIC's superior design freedom can enable applications beyond B_0 shimming through targeted
7 B_0 field shaping. It has the potential of providing a new hardware dimension for image encoding
8 and acceleration^{76,77}, B_1 correction⁷⁸, and FOV reduction⁷⁹.

9 By adding shimming capability into a conventional RF coil, UNIC functionalizes existing
10 MRI systems with minimal changes required to the current scanner architecture to significantly
11 extend its clinical compatibility. Our findings here are not unlike other historical advances in
12 MRI, which have been enabled by hardware improvements such as multichannel RF detection³¹
13 and transmission^{80,81}. In the same spirit, we envision that UNIC can be a major advancement
14 over the current (distant) B_0 shim coils to facilitate the introduction of a new generation of MR
15 coils with the improved B_0 shimming capability and high RF sensitivity.
16

17 **Methods:**

18 **Bench studies:**

19 Frequency spectrum (Fig. 2D): The circular RF loop, diameter 9.0 cm, was wound using tinned
20 copper wire (diameter 1.3 mm) and made resonant at 123.2 MHz using three evenly distributed
21 18 pf capacitors, including a variable capacitor. Following the circuit diagram (Fig. 2B), a UNIC
22 figure-8 shim circuit, comprising two 2-turn circular loops, 5.0 cm diameter, 3.0 cm center-to-
23 center (overlap ratio of 40%), was constructed using enameled copper wire (diameter 1.3 mm).
24 An RF choke inductor (0.6 μ H) was soldered into each circular shim loop. The blocking
25 capacitors C2 were each 150 pf. The resonant frequency response was measured using a
26 homemade S_{12} probe and the Agilent N9923A 4GHz RF vector network analyzer. S_{12} curve was
27 first measured with the RF loop alone. The UNIC figure-8 shim loop was then overlapped and
28 centered with the RF loop, causing a slight frequency shift to 122.9MHz. The RF loop was tuned
29 back into resonance at 123.2MHz by adjusting the variable capacitor in the loop, and the S_{12}
30 curve was measured again. Coil quality factor (Q) bench measurement: Two sets of
31 measurements were made at the bench to compare the coil quality factors of two shim-RF
32 designs (Fig. 3A), i.e., with and without applying UNIC decoupling. The network analyzer, the
33 9.0 cm circular RF loop, and the UNIC figure-8 shim loops comprising two 2-turn 5.0 cm
34 circular shim loops with an overlapping ratio of 40% were used. For comparison, two turns naïve
35 circular (not decoupled) shim loops were made with the same geometry as the UNIC shim loops
36 (5.0 cm diameter, overlapping ratio of 40%). UNIC shim loops and naïve shim loops with 1-3
37 turns were also made. For UNIC, 0, 1, 2 RF chokes (0.6 μ H each) were inserted into each
38 circular shim loop of 1, 2, 3 turns, respectively. The blocking capacitors were 150 pf in all the
39 cases for UNIC. Our simulations showed 2-turn UNIC loops could provide sufficient shim field
40 strengths for body shimming at 3.0T. The setup was configured by placing the shim loops
41 overlapped and centered with the RF loop. Two sets of measurements were performed with
42 identical geometry and positioning, except one with UNIC decoupling and the other without
43 UNIC decoupling (naïve). Q-ratios ($Q_{\text{unloaded}} / Q_{\text{loaded}}$) were measured in each case with different
44 separations between the shim and RF loops and with a different number of loop turns. To
45 measure loaded Q, the RF loop was located 1cm away from the side of a homemade cubic
46 phantom (1% NaCl doped water). The measurement setups were adjusted carefully to ensure a

1 fair comparison between UNIC and naïve coils. Conditions were kept consistent in the
2 comparison, including the S_{12} probe baseline <-70 dB, the S_{12} peak (21db), resonance frequency
3 at 123.2 MHz, frequency bandwidths set to 8.0 MHz and 30.0 MHz, respectively, for the
4 phantom unloaded and loaded. The S_{12} probe location relative to the RF loop and the RF loop
5 position relative to the phantom were kept as nearly identical as possible. Additionally,
6 precautions were taken to ensure that the baseline of the shim loops did not contaminate the S_{12}
7 spectrum. The separation between the shim loops and the RF loop was adjusted by using a small
8 amount of blue tack that had a negligible effect on the measurements. In all cases, the Q was
9 computed as the ratio of the measured resonance frequency divided by the measured frequency
10 bandwidth as 3dB below the resonance peak amplitude.

11 **Numerical simulations:**

12 Shim field strength and spatial variation: To investigate the shimming performance of UNIC, the
13 strength and spatial variation of the generated shim fields were simulated using the Biot-Savart
14 law for both UNIC coils and naïve coils (**Fig. 3**). The fields were simulated on an axis
15 perpendicular to the plane of the circular 2-turn shim loops at the center of symmetry of the coils
16 (central axis) and 1A shim currents. To compare coils with comparable RF performance, the
17 naïve coil was adopted with $\text{Gap}=2R_{\text{shim}}$ (Q-ratio $>80\%$ in **Fig. 3A**). The shim field strength from
18 each coil was simulated along the central axis for distances from zero up to $6R_{\text{shim}}$ away from the
19 coil plane. Field strength was normalized by the maximum field from the naïve coil. The
20 distance in the simulations was presented as multiples of the shim loop radius (R_{shim}). The spatial
21 variability of the shim fields was evaluated with the spatial derivatives (0-6th order) of the
22 simulated shim fields. The mean magnitude of the field's spatial derivatives in a defined ROI (1-
23 $3R_{\text{shim}}$ from the coil surface)⁴⁷ were computed. The ratio between the UNIC and naïve coils for
24 each derivative order ($\text{UNIC}^{(n)}\div\text{Naïve}^{(n)}$) was reported to evaluate the amplification of high-
25 order components with UNIC (**Fig. 3**). Susceptibility mismatch induced off-resonance frequency
26 map in the human body: Theoretical field inhomogeneity was evaluated using a numerical
27 simulation platform (Medical Interactive Creative Environment; MICE)⁸². Details of the
28 simulation are described in the supplementary material. In our study, a 3D volume covering the
29 torso of a human subject was created with comparable imaging parameters to the in-vivo scans.
30 To define the ROIs for evaluating B_0 homogeneity in the target organs, contours of the heart and
31 liver were depicted based on the input images. The root mean square error (RMSE) and median
32 (95% range) of the B_0 were measured in the heart and the liver and reported in the supplementary
33 material. All simulations were performed with in-house developed Matlab (Mathworks 2016R)
34 scripts. The simulation setups were applied for a 3.0T and 7.0T to examine the applicability of
35 UNIC in an ultra-high field environment and presented in the supplementary material. At 7.0T,
36 higher shim loop turns ($n=3$) were adopted to accommodate the amplified B_0 inhomogeneity.

37 **Prototype UNIC coil and hardware development:**

38 Coil design, shim-RF loop layout, and control system: A unified shim-RF coil system for body
39 imaging was built from the ground up. This consisted of a UNIC coil array and a shim current
40 driver and control system. The UNIC array was constructed with two flat sub-arrays, top and
41 bottom, each having 6 RF receive channels and 21 shim channels (**Fig. 4A.1**), for a total of 12
42 RF and 42 shim channels. The subject would position between the two flat sub-arrays, adjustable
43 in height to closely fit the subject for maximizing RF sensitivity and shim efficiency. The RF
44 array layout was similar to that of a conventional six-channel commercial body array (size 45.0
45 cm \times 30.0 cm). Two-turn shim loops (8.5 cm diameter, wire diameter 1.0 mm) were employed
46 for the first prototype, providing a sufficient field strength and reducing the maximum current to

1 5.0 A for minimal heating. For each of the top and bottom arrays, a total of six shim-RF coil
2 clusters were arranged in 2 rows of 3 clusters. Each cluster contains a 1-ch RF receive (Rx) loop
3 and a 2-ch 2-turn UNIC figure-8 shim loop. The Rx loop is overlapped with the figure-8 shim
4 loop. Additionally, either 4 or 5 shim loops skirt the edge of either row (**Fig. 4A1**). Between
5 nearest neighboring Rx loops, geometrical decoupling was applied. In addition, preamplifier
6 decoupling was used to decouple non-nearest neighboring Rx loops. Between the overlapping
7 shim and RF loops, the figure-8 geometrical decoupling was used (**Fig. 2**) in addition to RF
8 chokes to eliminate potential interference between shim loops and wires and their surrounding
9 Rx loops. The outermost nine shim loops had partial overlapping and were thus geometrically
10 decoupled from the respective Rx loops. Coil construction: The RF coil construction procedure
11 was similar to that of building a conventional RF array, which includes unloaded-to-loaded
12 quality factor ratio (Q-ratio) measurements during each step, tuning for active decoupling,
13 adjusting for preamplifier decoupling, tweaking for critical overlap geometrical decoupling,
14 array assembly, tuning and matching, and final bench touch up. The coil loading procedure used
15 a torso phantom mimicking the dielectric properties of the human body. Completion of the Rx
16 array was followed by adding shim loops & twisted DC wires to the respective Rx loops. RF
17 chokes need to be inserted in DC wires to prevent interference from the transmit RF field and to
18 minimize the RF coupling with the surroundings. It was noted that adding shim loops will cause
19 slight changes in the frequency and load conditions of the RF loops. Thus, a final round of
20 retuning and matching was needed for all Rx loops with a final check-up of their active detuning
21 and preamplifier decoupling. Cabling and interface: The design of shim current cabling followed
22 industrial safety standards. RF baluns every 20 cm along the cable were in place to eliminate
23 common mode currents during RF transmission. A 1.0 mm diameter DC wire was chosen to
24 allow 5.0 A maximum current without causing overheating. Additionally, RF filters in the shim
25 cable chains prevented RF noise propagation from shim circuits (outside of the MRI room) to RF
26 reception loops. The design and implementation of these filters were referred to as those for
27 conventional gradient and shim systems, where filters are installed on the wall between the MRI
28 room (where gradient/shim coils are) and the equipment room (where gradient/shim amplifiers
29 reside). Shim current driver system: A homemade multichannel DC current amplifier system
30 was constructed to independently drive currents to 42 shim coils with Arduino-based digital
31 control interfaces. The system was tested to supply up to ± 7.5 A DC current with $\pm 1.0\%$ error.
32 UNIC shim field measurement: In order to generate desired shim pattern, the shim field from
33 each of the 42 shim coils of the prototype array was measured separately with 1A shim current
34 sustained. B_0 field maps before and after applying the current were acquired for each shim
35 channel. The field differences were recorded as the unit shim field from each channel and were
36 used to calculate the shim currents during the UNIC shimming workflow sections in our
37 subsequent studies, detailed below. Safety evaluation: Prior to imaging humans, a series of
38 safety tests were performed on the bench and the scanner. The UNIC coil passed all the standard
39 RF coil safety tests⁸³, including the RF power absorption test in the detuned coil and coil heating
40 tests resulting from switched gradient and RF transmit power. The absorbed power was in the
41 normal range compared to the corresponding clinical coil. Both RF and gradient eddy current
42 effects were negligible on the local Rx and shim loops in agreement with previous studies^{18,44,45}.
43 In addition, for shim current-induced ohmic heating, we measured the temperature rise in the
44 shim circuitry on the bench by running the maximum shim currents 5.0 A through individual
45 channels. We also monitored the temperature increase within the entire array with 5.0 A in all
46 channels inside the magnet. The hot spot had a maximum temperature increase of less than 7 °C.

1 **Imaging studies:**

2 All imaging was performed at a 3.0T clinical scanner (Biograph mMR, Siemens Healthcare,
3 Erlangen, Germany). Image-based shimming was implemented with shim box selection to match
4 the target ROIs. Data analysis, numerical simulation, and image processing were done using
5 customized Matlab scripts. Imaging parameters from all MRI sequences are summarized in the
6 supplementary materials.

7 *Phantom scans:* To test the RF performance of the prototype array under a controlled
8 environment, experiments were performed in phantoms. A standard American College of
9 Radiology (ACR) phantom (cylindrical, 20.3cm x 17.3cm) and a larger body phantom
10 (rectangular, 40.0cm x 30.0cm x 20.0cm) were used to test the arrays' structure imaging ability
11 and spatial coverage. The constructed array was compared to a six-channel standard surface
12 array (BodyMatrix. Siemens Healthcare, Erlangen, Germany). Arrays were placed over the
13 phantoms using a rectangular rack to support the arrays and to keep the experimental setup
14 identical. The prototype and standard surface array were set up in consecutive imaging sessions.
15 After localization, images were acquired with a 3D proton density-weighted(PDW) gradient
16 recall echo (GRE) sequence to evaluate the SNR for each coil. PDW images were acquired with
17 the clinical RF array, the prototyped RF only array, and the prototyped UNIC array. SNR maps
18 were derived using the difference from two consecutive measurements^{84,85}. The SNR maps from
19 different arrays were compared using histogram analysis. To further test the noise characteristics
20 of the prototype arrays, noise covariance information was acquired using the same GRE
21 sequence without the excitation pulse. The coil noise correlation matrix was calculated for the
22 clinical RF array and the UNIC array³⁵. To examine the B_0 shimming capability of the
23 constructed UNIC prototype, a metallic off-resonance source (MO; a copper screwdriver) was
24 placed in the field of view (FOV) to emulate the high-order field inhomogeneity generated from
25 the tissue interfaces. The screwdriver was placed 5.0cm away from the ACR phantom to induce
26 a high-order off-resonance pattern. B_0 maps and clinical bSSFP images were acquired using both
27 the scanner shim alone and with UNIC shim to probe the B_0 shimming and imaging capability of
28 the constructed array. During scanning, the scanner 2nd SH B_0 shim and UNIC shim were applied
29 subsequently. First, scanner shim was applied to the ROIs with a standard image-based
30 shimming procedure⁴⁸. Shim volume was defined with a manually selected shim box to perform
31 shimming. Following the scanner shim and image acquisitions, UNIC shim was applied on top of
32 the scanner shim. The same shim volume and shimming process were used to derive the UNIC
33 shim field. The UNIC shim currents were calculated using linear least-square optimization. The
34 shim current for each UNIC channel was driven by a separate channel of a DC control system.
35 The optimization was constrained by maximum DC current $\pm 5.0A$ per coil. B_0 field maps and
36 bSSFP Images were acquired under each shimming condition. To compare the shimming
37 capability, a pixel-wise off-resonance field map was derived under each shimming condition.
38 Magnitude images from the sequence were used to define the ROIs for B_0 field analysis. Since
39 the field distribution is mostly skewed under the influence of the MO, histogram, RMSE,
40 median, and 95% range of the off-resonance maps were all measured.

41 *In-vivo human scans:* Healthy human volunteers (N=8; five female) were recruited to test the
42 ability of the constructed shim array in deep organs. Subjects were consented and the studies
43 were conducted in accordance with the Institutional Review Board requirements at Cedars-Sinai
44 Medical Center. The volunteers were scanned in the head-first supine position with the UNIC
45 double array (top and bottom). Localizers were acquired to determine the imaging planes and
46 shim volumes for B_0 shimming. The heart and liver were scanned in a randomized order in all

1 subjects. Before image acquisition, the scanner table was adjusted to move the target organs to
2 the center of the bore to facilitate optimized B₀ field homogeneity. Image Acquisition: The B₀
3 field maps were acquired in the target organs before and after applying the UNIC and scanner
4 shims. In addition, off-resonance sensitive sequences (bSSFP and EPI) were acquired to capture
5 the image quality differences under all shimming conditions. In the cardiac scans, high resolution
6 (1 x 1mm²) bSSFP cine images with extended TR (5.6ms) were acquired to evaluate the image
7 quality of the heart. Three short-axis slices (basal, mid, and apical) were acquired and analyzed.
8 In the liver scans, an EPI sequence and a bSSFP sequence were acquired. The images were
9 acquired in the coronal view to illustrate the off-resonance effect at the liver-lung interfaces.
10 Three imaging slabs with six slices each were used to cover different sections of the liver. In all
11 bSSFP images, frequency scouts were performed to optimize the image quality. Identical
12 imaging parameters were applied under the scanner shim and UNIC shim. All images were
13 acquired under breath holds. A similar shimming procedure as described in the ex-vivo studies
14 was used in the in-vivo studies. Shim volumes matching the image position were adopted for
15 each image acquisition. To minimize breathing motion-induced field disturbance, all B₀
16 shimming and imaging were performed at the end-expiration. The field of view and slice
17 coverage of the field maps were adjusted to cover the human liver and heart in each subject.
18 Image analysis: To evaluate B₀ homogeneity in the target organs, pixel-wise off-resonance maps
19 were derived with the same method described for the phantom study. Contours of the liver and
20 the heart were delineated using the magnitude images to refine the ROIs. The RMSE, median,
21 and 95% range of the off-resonance field in the target organs were derived to assess shimming
22 performances. All B₀ fields were tuned up to the central frequency of the target volume.
23 Quantitative comparison of scanner- and UNIC-shimmed fields were made in all volunteers. To
24 evaluate the quality of the images obtained with clinically relevant sequences, the image quality
25 scores were measured for the bSSFP images in both organs and EPI images in the liver. The
26 consensus was reached by two readers with 3+ years of experience. Image quality scores were
27 assigned according to the extent of artifacts using a 5-point ordinal scale as follows: 1 =
28 unreadable images, 2 = severe image artifacts, 3 = moderate image artifacts, 4 = minor image
29 artifacts, 5 = no image artifacts.

30 In-vivo animal scans: Dogs (n = 3, 22 to 26 kg) were studied with and without surgically
31 induced myocardial infarction (MI). All animals were studied according to the National Institutes
32 of Health (NIH) Guide for the Care and Use of Laboratory Animals following approval of the
33 Institutional Animal Care and Use Committee. To induce MI, animals underwent 3 hours of no-
34 flow ischemia followed by reperfusion, as described from a previous study⁵⁰ The animals were
35 scanned to test the cardiac shimming capability of the UNIC array. Cardiac MRI was performed
36 eight weeks after the infarction-reperfusion procedure. Image acquisition: Before all imaging
37 studies, animals were fasted, sedated, intubated, and anesthetized. During the imaging studies,
38 anesthesia was maintained with isoflurane. Dogs were transferred to the MR scanner table and
39 were mechanically ventilated. Hearts were localized, and baseline field maps were acquired for
40 B₀ shimming (similarly to the human studies). Also, similar to the human studies, Scanner shim
41 and UNIC shim were performed in sequential order. Under each shimming condition, B₀ field
42 maps and mid-ventricular short-axis T2* images (Gradient recall echo, TE=16.4ms) were
43 acquired. Afterward, late gadolinium enhancement (LGE) images, which are insensitive to B₀
44 off-resonance, were acquired under scanner shim to identify the location of the myocardial
45 infarction. Typical imaging parameters used were similar to human studies. Image analysis: To
46 test the influence of the blooming artifacts in detecting local myocardial iron deposition, T2*

1 images were analyzed with a standard procedure to identify hemorrhagic infarction⁸. Endocardial
2 and epicardial contours were first delineated in the T2* images. Remote myocardium was
3 identified as the region that showed no hyperintensity in the LGE images. The hemorrhagic
4 territories were identified in the myocardium with signal intensity 2 SD lower than the mean
5 signal intensity in the remote ROI.

6 7 **Statistical analyses:**

8 Differences between the RMSE, Median, and 95% range of the off-resonance fields were
9 analyzed using paired sample t-tests, and the image quality scores were compared using the
10 Wilcoxon rank-sum test. Value of $P < 0.05$ was considered statistically significant. Normality was
11 checked by the Shapiro-Wilk test.

12 13 **Acknowledgments**

14 This work was supported in part by NIH R01HL156818, NIH R01NS121544, NIH
15 U01EB028145, and NIH R01HL147133. We thank Q. Dong, Z. Wen, N. Zhang, K. Kwon, S.
16 Selvin, M. Strom, X. Li, Y. Shan, X. Mu, Y. Cai, G. Zhou, L. Zeng, E. Gutierrez, S.
17 Barzegarjalali, F. Xu, Y. Guo, X. Huang, N. She, Y. Liu, K. Tan, M. Lu, Z. Li, S. Guo, Y. Wang,
18 and M. Chen for assistance with UNIC hardware prototyping and software development; B.
19 Stoeckel, F. Han, X. Bi for help with coil files installation; F. Robb, M. Navarro, W. Shawn, E.
20 Gill, W. Tawackoli, L. Smith, Y. Zhang for helpful discussions.

21 22 **Author contributions**

23 H.H. conceived the concept, designed and constructed the UNIC coil, and supervised the work.
24 H.H., H.J.Y., F.M.S., P.H., H.S., J.S., W.L., R.H., and M.W. contributed to hardware prototyping
25 and software development. H.J.Y., Z.F., A.G.C., Y.X., R.D., D.L., and H.H. designed
26 experiments. H.J.Y., F.M.S., Z.F., N.W., A.K., Y.H., W.L., L.A., M.L., G.Y., and H.H.
27 performed experiments and/or analyzed the data. H.J.Y. and H.H. wrote the manuscript. All
28 authors contributed to editing and improving the manuscript.

29
30 **Correspondence and requests for materials** should be addressed to H.H., D.L., R.D., or M.W.

31 32 **Competing interests**

33 Cedars-Sinai has filed patent applications directed to this technology.

34 35 **List of Supplementary Materials**

36 S.1. Numerical simulation for theoretical shimming in deep organs

37 S.2. MRI imaging parameters

38 S.3. bSSFP Cine videos

References

- 1 Webb, A. G. *Magnetic resonance technology: hardware and system component design*. (Royal Society of Chemistry, 2016).
- 2 Vaughan, J. T. *et al.* Whole-body imaging at 7T: preliminary results. *Magnetic Resonance in Medicine: An Official Journal of the International Society for Magnetic Resonance in Medicine* **61**, 244-248 (2009).
- 3 Mullen, M. & Garwood, M. Contemporary approaches to high-field magnetic resonance imaging with large field inhomogeneity. *Progress in Nuclear Magnetic Resonance Spectroscopy* **120**, 95-108 (2020).
- 4 Atalay, M. K., Poncelet, B. P., Kantor, H. L., Brady, T. J. & Weisskoff, R. M. Cardiac susceptibility artifacts arising from the heart-lung interface. *Magn Reson Med* **45**, 341-345, doi:10.1002/1522-2594(200102)45:2<341::aid-mrm1043>3.0.co;2-q (2001).
- 5 Merkle, E. M. & Dale, B. M. Abdominal MRI at 3.0 T: the basics revisited. *American Journal of Roentgenology* **186**, 1524-1532 (2006).
- 6 Reeder, S. B., Faranesh, A. Z., Boxerman, J. L. & McVeigh, E. R. In vivo measurement of T² and field inhomogeneity maps in the human heart at 1.5 T. *Magn Reson Med* **39**, 988-998, doi:10.1002/mrm.1910390617 (1998).
- 7 Carr, J. C. *et al.* Cine MR angiography of the heart with segmented true fast imaging with steady-state precession. *Radiology* **219**, 828-834, doi:10.1148/radiology.219.3.r01jn44828 (2001).
- 8 Kali, A., Tang, R. L., Kumar, A., Min, J. K. & Dharmakumar, R. Detection of acute reperfusion myocardial hemorrhage with cardiac MR imaging: T2 versus T2. *Radiology* **269**, 387-395, doi:10.1148/radiol.13122397 (2013).
- 9 Meyer, C. H., Hu, B. S., Nishimura, D. G. & Macovski, A. Fast spiral coronary artery imaging. *Magn Reson Med* **28**, 202-213, doi:10.1002/mrm.1910280204 (1992).
- 10 Yang, H. J. *et al.* Free-breathing, motion-corrected, highly efficient whole heart T2 mapping at 3T with hybrid radial-cartesian trajectory. *Magn Reson Med* **75**, 126-136, doi:10.1002/mrm.25576 (2016).
- 11 Sun, C. *et al.* Non-Cartesian slice-GRAPPA and slice-SPIRiT reconstruction methods for multiband spiral cardiac MRI. *Magn Reson Med* **83**, 1235-1249, doi:10.1002/mrm.28002 (2020).
- 12 Muller, M. F. *et al.* Abdominal diffusion mapping with use of a whole-body echo-planar system. *Radiology* **190**, 475-478, doi:10.1148/radiology.190.2.8284402 (1994).
- 13 Bolan, P. J., Nelson, M. T., Yee, D. & Garwood, M. Imaging in breast cancer: magnetic resonance spectroscopy. *Breast Cancer Research* **7**, 1-4 (2005).
- 14 Cho, S. G. *et al.* Chronic hepatitis: in vivo proton MR spectroscopic evaluation of the liver and correlation with histopathologic findings. *Radiology* **221**, 740-746, doi:10.1148/radiol.2213010106 (2001).
- 15 Yang, H. J. *et al.* Accurate needle-free assessment of myocardial oxygenation for ischemic heart disease in canines using magnetic resonance imaging. *Sci Transl Med* **11**, doi:10.1126/scitranslmed.aat4407 (2019).
- 16 Taouli, B. & Koh, D. M. Diffusion-weighted MR imaging of the liver. *Radiology* **254**, 47-66, doi:10.1148/radiol.09090021 (2010).
- 17 Girometti, R., Maieron, M., Lissandrello, G., Bazzocchi, M. & Zuiani, C. Test-retest reliability of diffusion tensor imaging of the liver at 3.0 T. *Radiol Med* **120**, 489-497, doi:10.1007/s11547-014-0479-8 (2015).

1 18 Han, H., Song, A. W. & Truong, T. K. Integrated parallel reception, excitation, and
2 shimming (iPRES). *Magn Reson Med* **70**, 241-247, doi:10.1002/mrm.24766 (2013).

3 19 Winkler, S. A. *et al.* Gradient and shim technologies for ultra high field MRI.
4 *NeuroImage* (2016).

5 20 de Graaf, R. A. & Juchem, C. *B0 Shimming Technology. Book "Magnetic resonance*
6 *technology: hardware and system component design"*. 166-207 (Royal Society of
7 Chemistry, 2016).

8 21 Vannesjo, S. J. *et al.* Gradient and shim pre-emphasis by inversion of a linear time-
9 invariant system model. *Magnetic resonance in medicine* **78**, 1607-1622 (2017).

10 22 Boer, V. O., Klomp, D. W., Juchem, C., Luijten, P. R. & de Graaf, R. A. Multislice (1)H
11 MRSI of the human brain at 7 T using dynamic B(0) and B(1) shimming. *Magn Reson*
12 *Med* **68**, 662-670, doi:10.1002/mrm.23288 (2012).

13 23 Poole, M. & Bowtell, R. Volume parcellation for improved dynamic shimming. *Magnetic*
14 *Resonance Materials in Physics, Biology and Medicine* **21**, 31-40 (2008).

15 24 Schwerter, M. *et al.* Interslice current change constrained B0 shim optimization for
16 accurate high-order dynamic shim updating with strongly reduced eddy currents.
17 *Magnetic resonance in medicine* **82**, 263-275 (2019).

18 25 Wilson, J. L. & Jezzard, P. Utilization of an intra-oral diamagnetic passive shim in
19 functional MRI of the inferior frontal cortex. *Magnetic Resonance in Medicine: An*
20 *Official Journal of the International Society for Magnetic Resonance in Medicine* **50**,
21 1089-1094 (2003).

22 26 Sengupta, S. *et al.* Dynamic B0 shimming at 7 T. *Magnetic resonance imaging* **29**, 483-
23 496 (2011).

24 27 Hancu, I., Govenkar, A., Lenkinski, R. E. & Lee, S. K. On shimming approaches in 3T
25 breast MRI. *Magnetic resonance in medicine* **69**, 862-867 (2013).

26 28 Jia, F. *et al.* Design of a shim coil array matched to the human brain anatomy. *Magnetic*
27 *resonance in medicine* **83**, 1442-1457 (2020).

28 29 Golay, M. J. Field homogenizing coils for nuclear spin resonance instrumentation.
29 *Review of Scientific Instruments* **29**, 313-315 (1958).

30 30 Roméo, F. & Hoult, D. Magnet field profiling: analysis and correcting coil design.
31 *Magnetic Resonance in Medicine* **1**, 44-65 (1984).

32 31 Roemer, P. B., Edelstein, W. A., Hayes, C. E., Souza, S. P. & Mueller, O. The NMR
33 phased array. *Magnetic resonance in medicine* **16**, 192-225 (1990).

34 32 Uğurbil, K. *et al.* Brain imaging with improved acceleration and SNR at 7 Tesla obtained
35 with 64-channel receive array. *Magnetic resonance in medicine* **82**, 495-509 (2019).

36 33 Hennig, J. *et al.* 15 Years MR-encephalography. *MAGMA* **34**, 85-108,
37 doi:10.1007/s10334-020-00891-z (2021).

38 34 Sodickson, D. K. & Manning, W. J. Simultaneous acquisition of spatial harmonics
39 (SMASH): fast imaging with radiofrequency coil arrays. *Magnetic resonance in medicine*
40 **38**, 591-603 (1997).

41 35 Pruessmann, K. P., Weiger, M., Scheidegger, M. B. & Boesiger, P. SENSE: sensitivity
42 encoding for fast MRI. *Magn Reson Med* **42**, 952-962 (1999).

43 36 Hennig, J. *et al.* Parallel imaging in non-bijective, curvilinear magnetic field gradients: a
44 concept study. *Magnetic Resonance Materials in Physics, Biology and Medicine* **21**, 5
45 (2008).

1 37 Griswold, M. A. *et al.* Generalized autocalibrating partially parallel acquisitions
2 (GRAPPA). *Magn Reson Med* **47**, 1202-1210, doi:10.1002/mrm.10171 (2002).

3 38 Feinberg, D. A. *et al.* Multiplexed echo planar imaging for sub-second whole brain FMRI
4 and fast diffusion imaging. *PloS one* **5**, e15710 (2010).

5 39 Setsompop, K. *et al.* Blipped-controlled aliasing in parallel imaging for simultaneous
6 multislice echo planar imaging with reduced g-factor penalty. *Magn Reson Med* **67**,
7 1210-1224, doi:10.1002/mrm.23097 (2012).

8 40 Hsu, J. J. & Glover, G. H. Mitigation of susceptibility-induced signal loss in
9 neuroimaging using localized shim coils. *Magn Reson Med* **53**, 243-248,
10 doi:10.1002/mrm.20365 (2005).

11 41 Pan, J. W., Lo, K. M. & Hetherington, H. P. Role of very high order and degree B0
12 shimming for spectroscopic imaging of the human brain at 7 tesla. *Magn Reson Med* **68**,
13 1007-1017, doi:10.1002/mrm.24122 (2012).

14 42 Juchem, C., Nixon, T. W., McIntyre, S., Rothman, D. L. & de Graaf, R. A. Magnetic
15 field homogenization of the human prefrontal cortex with a set of localized electrical
16 coils. *Magn Reson Med* **63**, 171-180, doi:10.1002/mrm.22164 (2010).

17 43 Juchem, C. *et al.* Dynamic multi-coil shimming of the human brain at 7 T. *J Magn Reson*
18 **212**, 280-288, doi:10.1016/j.jmr.2011.07.005 (2011).

19 44 Truong, T. K., Darnell, D. & Song, A. W. Integrated RF/shim coil array for parallel
20 reception and localized B0 shimming in the human brain. *Neuroimage* **103**, 235-240,
21 doi:10.1016/j.neuroimage.2014.09.052 (2014).

22 45 Stockmann, J. P. *et al.* A 32-channel combined RF and B0 shim array for 3T brain
23 imaging. *Magn Reson Med* **75**, 441-451, doi:10.1002/mrm.25587 (2016).

24 46 Chang, P., Nassirpour, S. & Henning, A. J. M. r. i. m. Modeling real shim fields for very
25 high degree (and order) B0 shimming of the human brain at 9.4 T. **79**, 529-540 (2018).

26 47 Haase, A. *et al.* NMR probeheads for in vivo applications. *Concepts in Magnetic*
27 *resonance* **12**, 361-388 (2000).

28 48 Gruetter, R. & Boesch, C. Fast, noniterative shimming of spatially localized signals. In
29 vivo analysis of the magnetic field along axes. *Journal of Magnetic Resonance (1969)* **96**,
30 323-334 (1992).

31 49 Markl, M., Alley, M. T., Elkins, C. J. & Pelc, N. J. Flow effects in balanced steady state
32 free precession imaging. *Magn Reson Med* **50**, 892-903, doi:10.1002/mrm.10631 (2003).

33 50 Wang, G. *et al.* Influence of Myocardial Hemorrhage on Staging of Reperfused
34 Myocardial Infarctions With T2 Cardiac Magnetic Resonance Imaging: Insights Into the
35 Dependence on Infarction Type With Ex Vivo Validation. *JACC Cardiovasc Imaging* **12**,
36 693-703, doi:10.1016/j.jcmg.2018.01.018 (2019).

37 51 Cokic, I. *et al.* Iron-Sensitive Cardiac Magnetic Resonance Imaging for Prediction of
38 Ventricular Arrhythmia Risk in Patients With Chronic Myocardial Infarction: Early
39 Evidence. *Circ Cardiovasc Imaging* **8**, doi:10.1161/CIRCIMAGING.115.003642 (2015).

40 52 Bulluck, H. *et al.* Residual Myocardial Iron Following Intramyocardial Hemorrhage
41 During the Convalescent Phase of Reperfused ST-Segment-Elevation Myocardial
42 Infarction and Adverse Left Ventricular Remodeling. *Circ Cardiovasc Imaging* **9**,
43 doi:10.1161/CIRCIMAGING.116.004940 (2016).

44 53 Moon, B. F. *et al.* Iron imaging in myocardial infarction reperfusion injury. *Nat Commun*
45 **11**, 3273, doi:10.1038/s41467-020-16923-0 (2020).

1 54 Carpenter, J. P. *et al.* On T2* magnetic resonance and cardiac iron. *Circulation* **123**,
2 1519-1528, doi:10.1161/CIRCULATIONAHA.110.007641 (2011).

3 55 Rajiah, P. & Bolen, M. A. Cardiovascular MR imaging at 3 T: opportunities, challenges,
4 and solutions. *Radiographics* **34**, 1612-1635, doi:10.1148/rg.346140048 (2014).

5 56 Noeske, R., Seifert, F., Rhein, K. H. & Rinneberg, H. Human cardiac imaging at 3 T
6 using phased array coils. *Magn Reson Med* **44**, 978-982, doi:10.1002/1522-
7 2594(200012)44:6<978::aid-mrm22>3.0.co;2-9 (2000).

8 57 Huang, S. Y. *et al.* Body MR Imaging: Artifacts, k-Space, and Solutions-Erratum.
9 *Radiographics* **35**, 1624, doi:10.1148/rg.2015154016 (2015).

10 58 Lewis, S., Dyvorne, H., Cui, Y. & Taouli, B. Diffusion-weighted imaging of the liver:
11 techniques and applications. *Magn Reson Imaging Clin N Am* **22**, 373-395,
12 doi:10.1016/j.mric.2014.04.009 (2014).

13 59 Girometti, R. 3.0 Tesla magnetic resonance imaging: A new standard in liver imaging?
14 *World J Hepatol* **7**, 1894-1898, doi:10.4254/wjh.v7.i15.1894 (2015).

15 60 Alam, M. H. *et al.* Comparison of 3 T and 1.5 T for T2* magnetic resonance of tissue
16 iron. *J Cardiovasc Magn Reson* **18**, 40, doi:10.1186/s12968-016-0259-9 (2016).

17 61 Kali, A. *et al.* Chronic manifestation of postreperfusion intramyocardial hemorrhage as
18 regional iron deposition: a cardiovascular magnetic resonance study with ex vivo
19 validation. *Circ Cardiovasc Imaging* **6**, 218-228,
20 doi:10.1161/CIRCIMAGING.112.000133 (2013).

21 62 Ferreira, P. F., Gatehouse, P. D. & Firmin, D. N. Myocardial first-pass perfusion imaging
22 with hybrid-EPI: frequency-offsets and potential artefacts. *J Cardiovasc Magn Reson* **14**,
23 44, doi:10.1186/1532-429X-14-44 (2012).

24 63 Yang, H. J. *et al.* Heart Rate-Independent 3D Myocardial Blood Oxygen Level-
25 Dependent MRI at 3.0 T with Simultaneous (13)N-Ammonia PET Validation. *Radiology*
26 **295**, 82-93, doi:10.1148/radiol.2020191456 (2020).

27 64 Van Zijl, P. C. & Yadav, N. N. Chemical exchange saturation transfer (CEST): what is in
28 a name and what isn't? *Magnetic resonance in medicine* **65**, 927-948 (2011).

29 65 El-Sharkawy, A. M., Schar, M., Ouwerkerk, R., Weiss, R. G. & Bottomley, P. A.
30 Quantitative cardiac 31P spectroscopy at 3 Tesla using adiabatic pulses. *Magn Reson*
31 *Med* **61**, 785-795, doi:10.1002/mrm.21867 (2009).

32 66 Puntmann, V. O. *et al.* Native T1 mapping in differentiation of normal myocardium from
33 diffuse disease in hypertrophic and dilated cardiomyopathy. *JACC Cardiovasc Imaging*
34 **6**, 475-484, doi:10.1016/j.jcmg.2012.08.019 (2013).

35 67 Karamitsos, T. D. *et al.* Noncontrast T1 mapping for the diagnosis of cardiac
36 amyloidosis. *JACC Cardiovasc Imaging* **6**, 488-497, doi:10.1016/j.jcmg.2012.11.013
37 (2013).

38 68 Usman, A. A. *et al.* Cardiac magnetic resonance T2 mapping in the monitoring and
39 follow-up of acute cardiac transplant rejection: a pilot study. *Circ Cardiovasc Imaging* **5**,
40 782-790, doi:10.1161/CIRCIMAGING.111.971101 (2012).

41 69 Verhaert, D. *et al.* Direct T2 quantification of myocardial edema in acute ischemic injury.
42 *JACC Cardiovasc Imaging* **4**, 269-278, doi:10.1016/j.jcmg.2010.09.023 (2011).

43 70 Kellman, P., Herzka, D. A., Arai, A. E. & Hansen, M. S. Influence of Off-resonance in
44 myocardial T1-mapping using SSFP based MOLLI method. *J Cardiovasc Magn Reson*
45 **15**, 63, doi:10.1186/1532-429X-15-63 (2013).

- 1 71 Corea, J. R. *et al.* Screen-printed flexible MRI receive coils. *Nat Commun* **7**, 10839,
2 doi:10.1038/ncomms10839 (2016).
- 3 72 Zhang, B., Sodickson, D. K. & Cloos, M. A. A high-impedance detector-array glove for
4 magnetic resonance imaging of the hand. *Nat Biomed Eng* **2**, 570-577,
5 doi:10.1038/s41551-018-0233-y (2018).
- 6 73 Cogswell, P. M. *et al.* Application of Adaptive Image Receive Coil Technology for
7 Whole-Brain Imaging. *American Journal of Roentgenology* **216**, 552-559 (2021).
- 8 74 Yan, X., Gore, J. C. & Grissom, W. A. Self-decoupled radiofrequency coils for magnetic
9 resonance imaging. *Nat Commun* **9**, 3481, doi:10.1038/s41467-018-05585-8 (2018).
- 10 75 Larson, A. C. *et al.* Preliminary investigation of respiratory self-gating for free-breathing
11 segmented cine MRI. *Magn Reson Med* **53**, 159-168, doi:10.1002/mrm.20331 (2005).
- 12 76 Juchem, C. *et al.* Dynamic multicoil technique (DYNAMITE) MRI on human brain.
13 *Magn Reson Med* **84**, 2953-2963, doi:10.1002/mrm.28323 (2020).
- 14 77 Dispenza, N. L., Littin, S., Zaitsev, M., Constable, R. T. & Galiana, G. Clinical Potential
15 of a New Approach to MRI Acceleration. *Sci Rep* **9**, 1912, doi:10.1038/s41598-018-
16 36802-5 (2019).
- 17 78 Umesh Rudrapatna, S., Juchem, C., Nixon, T. W. & de Graaf, R. A. Dynamic multi-coil
18 tailored excitation for transmit B1 correction at 7 Tesla. *Magn Reson Med* **76**, 83-93,
19 doi:10.1002/mrm.25856 (2016).
- 20 79 Witschey, W. R. *et al.* Localization by nonlinear phase preparation and k-space trajectory
21 design. *Magn Reson Med* **67**, 1620-1632, doi:10.1002/mrm.23146 (2012).
- 22 80 Katscher, U., Börnert, P., Leussler, C. & Van Den Brink, J. S. Transmit sense. *Magnetic
23 Resonance in Medicine: An Official Journal of the International Society for Magnetic
24 Resonance in Medicine* **49**, 144-150 (2003).
- 25 81 Vaughan, T. *et al.* 9.4 T human MRI: preliminary results. *Magnetic Resonance in
26 Medicine: An Official Journal of the International Society for Magnetic Resonance in
27 Medicine* **56**, 1274-1282 (2006).
- 28 82 Lundman, J. A., Bylund, M., Garpebring, A., Karlsson, C. T. & Nyholm, T. Patient-
29 induced susceptibility effects simulation in magnetic resonance imaging. *Physics and
30 Imaging in Radiation Oncology* **1**, 41-45 (2017).
- 31 83 Keil, B. *et al.* A 64-channel 3T array coil for accelerated brain MRI. *Magn Reson Med*
32 **70**, 248-258, doi:10.1002/mrm.24427 (2013).
- 33 84 Reeder, S. B. *et al.* Practical approaches to the evaluation of signal-to-noise ratio
34 performance with parallel imaging: application with cardiac imaging and a 32-channel
35 cardiac coil. *Magn Reson Med* **54**, 748-754, doi:10.1002/mrm.20636 (2005).
- 36 85 Dietrich, O., Raya, J. G., Reeder, S. B., Reiser, M. F. & Schoenberg, S. O. Measurement
37 of signal-to-noise ratios in MR images: influence of multichannel coils, parallel imaging,
38 and reconstruction filters. *J Magn Reson Imaging* **26**, 375-385, doi:10.1002/jmri.20969
39 (2007).

40

41

42

1 **Supplementary Materials**

2
3 S.1. Numerical simulation for theoretical shimming in deep organs

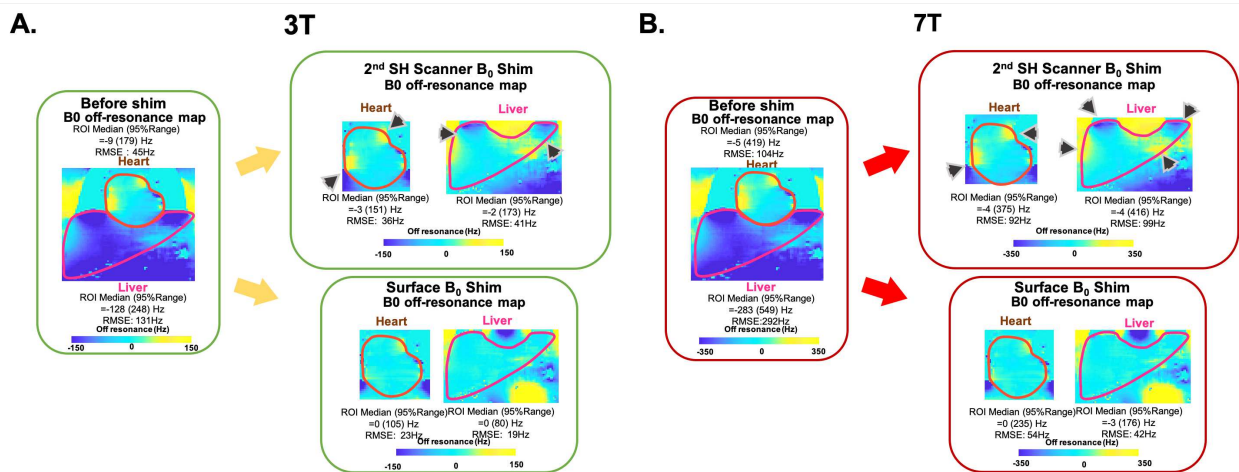
4
5 S.2. MRI imaging parameters

6
7 S.3. bSSFP Cine videos

8 9 **S.1. Numerical simulation for theoretical shimming in deep organs**

10 To investigate the theoretical shimming capability of the local shim loops and facilitate the
11 design of the body UNIC coil layout, numerical simulations of the B_0 off-resonance maps were
12 conducted using a digital human subject under high-field environments. The shimming
13 performance of a pair of 2 slab local shim arrays was compared to a 2nd order SH shim coil in the
14 scanner bore (equipped in the state-of-the-art clinical scanners). B_0 shimming was performed in
15 the heart and liver. The virtual magnetic field in a human body was simulated using a
16 simulation platform (Medical Interactive Creative Environment; MICE)¹. The B_0 field of the
17 thorax and abdominal region in a male subject was simulated based on the local magnetic shifts
18 from Lorentz sphere correction in the Fourier domain². Specifically, whole-body CT images
19 from a public dataset³ were used to generate the anatomy of the human body for the MICE
20 simulation. Thorax and abdominal slices were extracted for susceptibility map generation.
21 Hounsfield units of the CT images were used to define the tissue compositions in tissues¹, and
22 the corresponding susceptibility was assigned. Subsequently, the susceptibility maps were used
23 as an input for the Induced Susceptibility Effect Module to generate local B_0 field based on the
24 defined B_0 field strength (3.0T or 7.0T). A 3D volume covering the torso of the subject was
25 created with a comparable imaging parameter to the in-vivo scans
26 (FOV=39.7cm×26.2cm×39.5cm, resolution= 0.97mm×0.97mm×3.27mm). The B_0 field maps
27 were exported to perform B_0 shimming from different coils. To perform proper virtual B_0
28 shimming, shim fields from a scanner 2nd SH shim coil and local shim coil arrays were generated
29 using the biot-savart law. To represent realistic shim coil arrays, shim loops with 6.0cm
30 diameters were used to compose two coil arrays with a 30.0cm x 30.0cm surface area. 30.0cm
31 separation was adopted to fit the digital subject. The coils were aligned to the center of the
32 scanner and matching the location of the virtual subject. B_0 shim fields from the shim coils were
33 derived with a linear least-squares optimization algorithm that was the same as the in-vivo
34 studies. To perform proper shimming to the target organs, shim volumes were selected to only
35 cover the tightly covering the targeted regions. The B_0 fields generated by the 2nd SH and UNIC
36 coils were then applied to the digital phantom with a linear combination. The field
37 homogeneities in the target organs were evaluated by the root mean square error (RMSE) and
38 median (95%range) of the B_0 field in the heart and the liver. The simulation was performed
39 under 3.0T and 7.0T field strength to examine the theoretical performance of local shim arrays in
40 the high-field environments. Under 3.0T, a 50 channel shim array with evenly distributed two-
41 turn shim loops was used with 5.0A current limitations. Under 7.0T, three turn coils (1.5x max
42 shim field strength) were adopted to accommodate the amplified field inhomogeneity. All
43 simulations and analyses were performed with in-house developed MATLAB scripts. The
44 improved local shimming capability of the surface shim coil was tested in numerical simulation.
45 Results are presented in Fig. S1. B_0 fields in the heart and liver from a virtual patient were
46 analyzed. B_0 field maps from at 3.0T were shown in panel A. Comparing to the original shim

1 field without B_0 shimming, B_0 homogeneity was improved under both shimming conditions.
 2 Yet, a strong off-resonance field was measured at the tissue-lung interfaces after 2nd SH
 3 shimming in both organs (black arrows). Facilitated by the closed-up shim loops, a substantially
 4 more homogeneous B_0 field was measured after UNIC shim. (Field distribution at 3.0T (Median
 5 (95%Range) Hz) in the heart: Before shim:-9(179) Hz; 2nd SH: -3(151) Hz; Surface shim: 0(105)
 6 Hz; and liver: Before shim:-128(248) Hz; 2nd SH: -2(173) Hz; Surface shim: 0(80) Hz). Similar
 7 results in a simulation under ultrahigh-field (7.0T) are presented in panel B. (Field distribution at
 8 7.0T in the heart: Before shim:-5(419) Hz; 2nd SH: -4(375) Hz; Surface shim: 0(235) Hz; and
 9 liver: Before shim: -283(549) Hz; 2nd SH: -4(416) Hz; Surface shim: -3(176) Hz). The
 10 significantly improved shim field at 7T demonstrates the potential application of UNIC in
 11 ultrahigh-field body MRI.



12
 13 **Figure S1. Numerical simulation of deep tissue shimming with surface shim coils at high**
 14 **field environments.** The B_0 field map of a virtual patient was shimmed by a standard 2nd order
 15 SH in bore shim coil and 50 channel surface shim coils. B_0 homogeneity was improved under
 16 both shimming conditions compare to the original field. Substantially more homogeneous fields
 17 in the heart and liver were achieved under surface shim at 3T(A) and 7T(B).

19 S.2. MRI Imaging parameters

20 Phantom studies:

21 B_0 field maps: A dual-echo GRE sequence was used to derive B_0 field maps. Images were
 22 acquired with axial view using the following parameters: FOV : $40 \times 30 \times 36\text{cm}^3$; matrix size =
 23 112×84 ; in-plane resolution = 3.5×3.5 mm; slice thickness = 6 mm; TR/TE1/TE2 = 6.1 ms/2.5
 24 ms/4.8 ms; flip angle = 12° ; readout bandwidth = 795 Hz/Px;

25 SNR measurements: A GRE sequence was used to derive SNR maps. Images were acquired with
 26 coronal view using the following parameters: FOV : 50×50 cm²; matrix size = 512×512 ; in-
 27 plane resolution = 1.0×1.0 mm; slice thickness = 10 mm; TR/TE = 8.6 ms/4 ms; flip angle =
 28 20° ; readout bandwidth = 320 Hz/Px; Number of repetition=2.

29 bSSFP : A bSSFP sequence was used to acquire structural images. Images were acquired with
 30 axial view using the following parameters: FOV : 260×272 mm; matrix size = 260×272 ; in-
 31 plane resolution = 1.5×1.5 mm; slice thickness = 5 mm; TR/TE = 3.0 ms/1.5 ms; flip angle =
 32 30° ; readout bandwidth = 1000 Hz/Px; iPAT=2;

33 Human studies:

34 All in-vivo images were acquired under breath holds and at the end-expiratory phase.

1 B₀ field maps: B₀ field maps: A dual-echo GRE sequence was used to derive B₀ field maps.
2 Images were acquired with axial view using the following parameters: FOV : 40 × 30 cm³;
3 matrix size = 112 × 84; in-plane resolution = 3.5 × 3.5 mm; slice thickness = 6 mm;
4 TR/TE1/TE2 = 6.1 ms/2.5 ms/4.8 ms; flip angle = 12°; readout bandwidth = 795 Hz/Px; slice
5 numbers were adjusted according to the field of view.
6 Cardiac Cine: A bSSFP sequence with extended TR and high resolution was used to acquire cine
7 images of the heart. Images were acquired with axial view using the following parameters:
8 FOV : 260 × 272 mm; matrix size = 260 × 272; in-plane resolution = 1.0 × 1.0 mm; slice
9 thickness = 5 mm; TR/TE = 5.6 ms/2.9 ms; flip angle = 30°; readout bandwidth = 430 Hz/Px;
10 iPAT=2; retrospective cardiac gating was adopted.
11 Liver bSSFP : A bSSFP sequence was used to acquire anatomical liver images. Images were
12 acquired with axial view using the following parameters: FOV : 260 × 272 mm; matrix size =
13 260 × 272; in-plane resolution = 1.5 × 1.5 mm; slice thickness = 5 mm; TR/TE = 3.0 ms/1.5 ms;
14 flip angle = 30°; readout bandwidth = 1000 Hz/Px; iPAT=2;
15 Liver EPI: Coronal view Echo planer imaging; FOV = 307 × 379 mm; matrix size = 204 × 272;
16 in-plane resolution = 1.5 × 1.5 mm; slice thickness = 8 mm; Echo train length=51; EPI
17 factor=144; TR/TE = 1.8 s/54 ms; flip angle = 90°; readout bandwidth = 2205 Hz/Px; iPAT=2;
18 slice number =6; Fat suppressed;

19 Animal studies:

20 Cardiac T2* MRI: T2* images were acquired from short axis GRE images with TR= 149 ms,
21 TEs = 16.4ms, flip angle 10°, and bandwidth 1030 Hz/pixel. Voxel size for all acquisitions was
22 fixed to 1.5×1.5×8mm³
23 LGE: Typically used LGE imaging parameters were Axial view gradient-echo images, TR/TE=
24 750ms/1.6ms, TI= 300ms, flip angle 20°, and bandwidth= 465 Hz/pixel. Voxel size for all
25 acquisitions was fixed to 1.5×1.5×8mm³

26
27

28 **S.3. bSSFP Cine videos**

29 Files attached

30

31 **Supplementary References**

- 32 1 Lundman, J. A., Bylund, M., Garpebring, A., Karlsson, C. T. & Nyholm, T. Patient-
33 induced susceptibility effects simulation in magnetic resonance imaging. *Physics and Imaging in*
34 *Radiation Oncology* **1**, 41-45 (2017).
35 2 de Rochefort, L. *et al.* In vivo quantification of contrast agent concentration using the
36 induced magnetic field for time-resolved arterial input function measurement with MRI. *Medical*
37 *physics* **35**, 5328-5339 (2008).
38 3 Ackerman, M. J. The Visible Human Project: a resource for anatomical visualization.
39 *Stud Health Technol Inform* **52 Pt 2**, 1030-1032 (1998).

40

Supplementary Files

This is a list of supplementary files associated with this preprint. Click to download.

- [CineScannerrshim.avi](#)
- [CineUNICShim.avi](#)